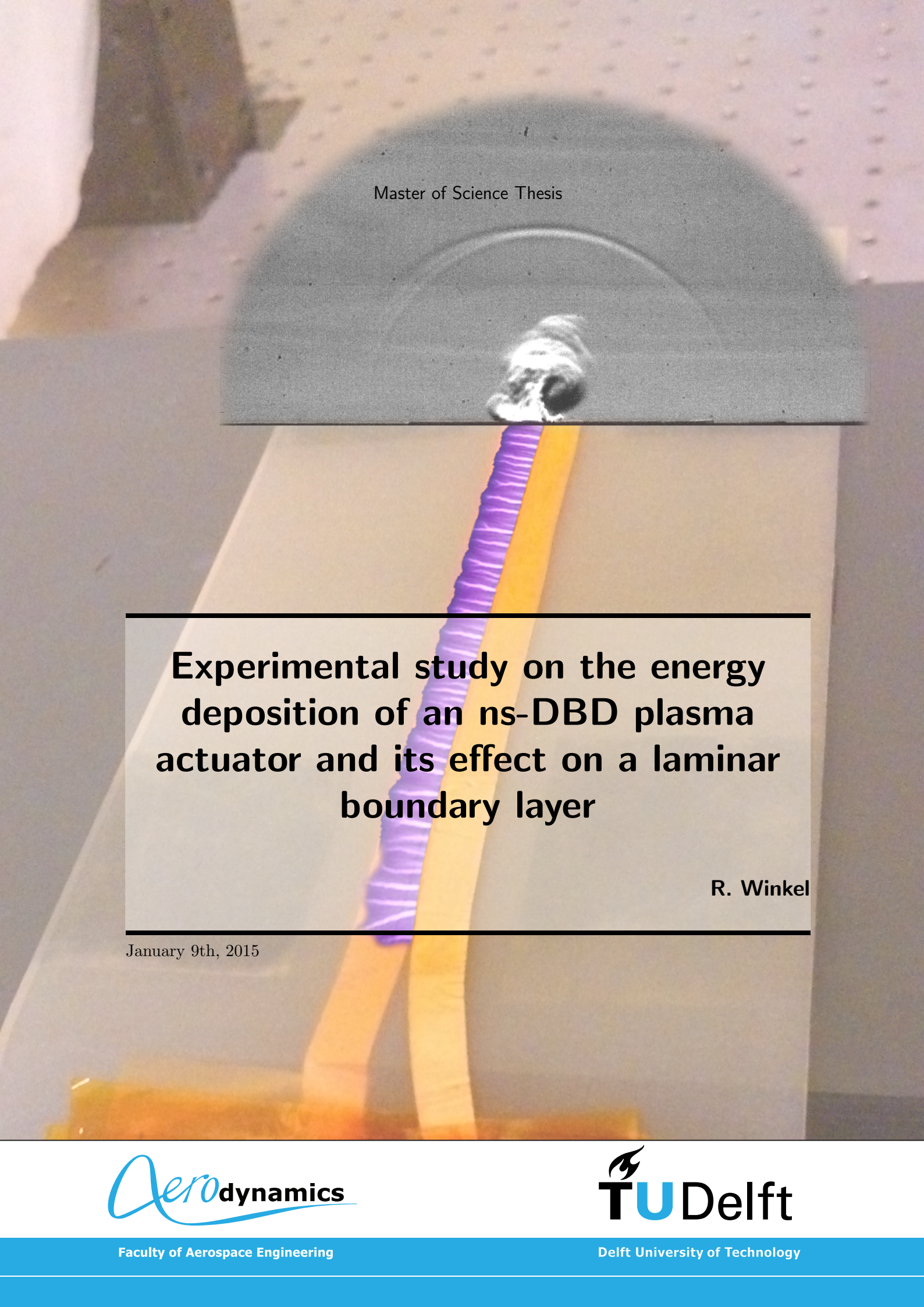


Master of Science Thesis



**Experimental study on the energy
deposition of an ns-DBD plasma
actuator and its effect on a laminar
boundary layer**

R. Winkel

January 9th, 2015

Experimental study on the energy deposition of an ns-DBD plasma actuator and its effect on a laminar boundary layer

Master of Science Thesis

For obtaining the degree of Master of Science in Aerospace Engineering
at Delft University of Technology

R. Winkel

January 9th, 2015



Delft University of Technology

Copyright © Aerospace Engineering, Delft University of Technology
All rights reserved.

DELFT UNIVERSITY OF TECHNOLOGY
DEPARTMENT OF AERODYNAMICS

The undersigned hereby certify that they have read and recommend to the Faculty of Aerospace Engineering for acceptance the thesis entitled “**Experimental study on the energy deposition of an ns-DBD plasma actuator and its effect on a laminar boundary layer**” by **R. Winkel** in fulfillment of the requirements for the degree of **Master of Science**.

Dated: January 9th, 2015

Supervisors:

Prof. Dr. F. Scarano

Dr. M. Kotsonis

Ir. G. Correale

Dr. D. Ragni

Preface

This report represents the final thesis which completes the master track of Aerodynamics and with which the Master's Degree in Aerodynamics could be obtained. Readers are expected to have reasonable knowledge in the field of aerodynamics.

Gratitude goes to Giuseppe Correale PhD. for his daily supervision and Dr. Marios Kotsonis for the healthy discussions. Technical support provided by Nico van Beek, Frits Donker-Duyvis and Peter Duynham was essential to succes of the experiments carried out within the context of this thesis. Support from the NovAM department of the faculty of Aerospace Engineering was provided by Hamideh Khanbareh and Nan Zhong.

Also a big thank you goes to my parents Hans and Nel Winkel for giving me the possibility graduate as an Aerospace Engineer.

Summary

Dielectric barrier discharge (DBD) plasma actuators have been a topic of academic investigations for the last few decades [Moreau (2007), Corke et al. (2009)]. The nanosecond pulsed dielectric barrier discharge (ns-DBD) plasma actuator is one of the more recent type of actuator in this field of study. Numerical and experimental studies have shown that this actuator affects the near wall volume of air with a small body force [Roupassov et al. (2009), Little et al. (2012)], a weak compression wave [Roupassov et al. (2009), Little et al. (2012), Benard et al. (2012)] and an overheating in the discharge region [Roupassov et al. (2009), Little et al. (2012), Correale et al. (2014)]. Roupassov et al. (2009) hypothesized that the main mechanism of impact for this actuator is the energy transfer to and the heating of the near-surface gas layer. However, this transfer of energy and the coupling to the local flow instabilities remain topics of interest. Additionally, structured experiments concerning the influence of the barrier on the thermal energy deposition to the near wall volume of air by discharge of an ns-DBD plasma actuator have as far known not been performed yet.

Fundamental understanding of the working principles of an ns-DBD plasma actuator is of importance for the improvement of the technology, such that it can be used outside of a controlled lab environment. The aim of this study is to uncover the influence of the barrier of an ns-DBD plasma actuator on the energy deposition to the near wall volume of air. Additionally, the effect of a tested ns-DBD plasma actuator on a laminar boundary layer is investigated.

Chosen barrier materials, that are used in this study, are Kapton[®] Polyimide tape, silicone-rubber and fine Polyamide PA2200. Thermal energy deposition effects in the near wall volume by discharge with these barriers has been investigated with the use of Schlieren measurements in quiescent conditions. Electrical energy measurements were made with the back-current shunt technique. Moreover, discharge characterization, on both morphology and intensity, has been done with direct imaging of the discharge. Additionally, the effect of an ns-DBD plasma actuator with a 2 layer Kapton tape barrier on a low velocity laminar boundary layer has been investigated with the use of phase-locked planar Particle Image Velocimetry (PIV). A backward-time backward-space finite difference discretization of the compressible continuity equation was proposed to quantify the density field disturbance ns-DBD plasma actuator. This method was validated in this study with experimental Schlieren images to give a reasonable approximation of the density field under the tested conditions.

Results of this study indicate that with equal energy input to an ns-DBD plasma actuator with a barrier of the same material, a thinner barrier will allow more thermal energy to be deposited per discharge pulse than a thicker barrier. This is caused by the smaller distance between the electrodes, which produces a stronger reduced electric field and a stronger discharge. Additionally, large differences in density gradient field disturbance and discharge structure are present between the tested materials.

Velocity field disturbance results indicate a strong dependence on stream wise position of the covered high voltage electrode relative to the exposed electrode. The low velocity laminar boundary layer experiences a local deceleration/acceleration of about $0.5 [m/s]$ in upstream/downstream position of the covered high voltage electrode. These results indicate the presence of a small body force directed from the exposed electrode to the covered HV electrode. Additionally, differences in magnitude of deceleration and acceleration are accredited to an induced viscosity gradient at the wall. Moreover, independent of the streamwise position of the covered high voltage electrode the effect of energy input is a local decrease in density. A larger area of density decrease is observed for the ns-DBD plasma actuator with the covered HV electrode in upstream position compared to the downstream position.

It can be concluded that a barrier used in an ns-DBD plasma actuator should have a low thickness, high electrical volume resistivity, low thermal capacitance and low heat capacity in order to efficiently deposit heat to the nearby air. Velocity field disturbances by ns-DBD plasma actuation in a laminar boundary layer indicated that the streamwise orientation of the electrodes is capable of inducing different velocity fields. Based on the density perturbation fields, these velocity fields are capable of enhancing the impact of the thermal energy deposition through better distribution through the boundary layer. A direct comparison between an ns-DBD plasma actuator and a pulsed wall or near-wall-volume heating device will increase the understanding of the influence of the body force on the thermal energy deposition for the flow control capabilities of ns-DBD plasma actuators.

Contents

Preface	v
Summary	vii
List of Figures	xiii
List of Tables	xvii
Nomenclature	xix
1 Introduction	1
2 Background	3
2.1 Boundary layer theory	3
2.2 Dielectric Barrier Discharge actuators	4
2.2.1 ns-DBD plasma actuator	5
Thermal energy deposition	6
Body force	7
Weak compression wave	8
2.2.2 Barrier materials	9
2.3 Boundary layer thermalization effects by non-plasma actuation.	10

2.3.1	Wall temperature control	10
2.3.2	Volumetric temperature control	10
2.4	Discussion	11
3	Experimental setup	13
3.1	ns-DBD plasma actuator	13
3.2	Schlieren imagery	16
3.3	Discharge characterization	17
3.4	Wind tunnel facility	18
3.5	Boundary layer model	18
3.6	Particle Image Velocimetry	19
3.7	Energy measurements	21
3.8	Barrier material tests	22
4	Barrier material dependent energy deposition	25
4.1	Barrier material specifications	25
4.2	Schlieren results	27
4.3	Discharge characterization	29
4.4	Volumetric heating by ns-DBD plasma discharge	31
4.5	Energy measurements	35
4.6	Discussion	38
5	Laminar boundary layer flow disturbance	41
5.1	Discretization of the compressible mass continuity equation	41
5.2	Particle Image Velocimetry results	42
5.2.1	Undisturbed velocity field	42
5.2.2	Disturbance by ns-DBD in a laminar boundary layer	44
5.3	Energy measurements	50

Contents	xi
5.4 Density method validation and results	51
5.5 Discussion	55
6 Conclusions and Recommendations	57
6.1 Conclusions	57
6.2 Recommendations	59
Bibliography	61

List of Figures

2.1	Schematic representation of a DBD plasma actuator in side view. Indicated are the electrode widths (w_1 , w_2), electrode thickness (t_e), barrier thickness (t_d) and inter electrode gap (g_e) [Correale et al. (2014)].	6
2.2	Thermal energy deposition effect by ns-DBD plasma actuator.	7
2.3	Induced velocities for ns-DBD plasma actuators.	8
2.4	Induced shock wave 10 [μs] after discharge at +10 [kV]. Scale in mm , with indicated pulse width (PW) [Benard et al. (2012)].	9
3.1	Schematic representation of an ns-DBD plasma actuator, viewed along the electrodes. Different scaling is used for x- and y-direction for better clarity. . . .	14
3.2	Schematic representation of an ns-DBD plasma actuator, shown in top view. . .	15
3.3	Schematic representation of an ns-DBD plasma actuator in the groove of the boundary layer model in the W-tunnel. Displayed configuration shows the covered high voltage electrode in downstream streamwise position. Different scaling is used for x- and y-direction for better clarity.	16
3.4	Schematic representation of the z-type Schlieren set-up.	17
3.5	Schematic representation of the setup for discharge imaging.	18
3.6	Schematic representation of the boundary layer model, with exaggerated ns-DBD plasma actuator and groove scaling for clarity.	19
3.7	Schematic representation of the setup with the boundary layer model in the W-tunnel. Size of the ns-DBD plasma actuator and laser sheet optics exaggerated for clarity.	20
3.8	Photograph of the setup with the boundary layer model in the transparent test section of the W-tunnel.	20
3.9	Scheme of acquisition timing in the PIV experiment. The example shows a discharge burst of 5 pulses with image acquisition 0 [ms] after the discharge burst has ended.	21

3.10	Measurement setups for the tested barriers material properties.	23
4.1	Measured barrier material properties.	27
4.2	Evolution of the disturbance in quiescent conditions shown by Schlieren density gradients normal to the wall. Difference to undisturbed density gradient field is visualized 0 [ms] after a discharge burst at 10 [kHz] for the three tested materials.	29
4.3	Characterization of the discharge structure of the three materials, tested at 1 [kHz] with an exposure time of 1 [s].	30
4.4	Average discharge light intensity of the three materials, measured over the middle 50 [mm] of the discharge. Results at 0.1 and 1 [kHz] with an exposure time of 1 [s].	31
4.5	Demonstration of the area measurement technique used for the Schlieren experiments. Interrogated image on the left, determined disturbed area in white on the right.	32
4.6	Growth of the disturbed density field area (A) over time with different amount of pulses. Results for the three tested barrier materials at their three tested barrier thicknesses. Discharge pulses at 10 [kV] and a frequency of 10 [kHz].	33
4.7	The area of the disturbed density field area over the three thicknesses for the three different barrier materials tested. Area measured directly after the application of the last discharge pulse. Discharge pulses at 10 [kV] and a frequency of 10 [kHz].	34
4.8	The ratio of disturbed area to the thickness of the barrier for the first 10 [μs] of the experiment for the three different barrier materials tested. Data of a discharge burst of 30 pulses is shown. Discharge pulses at 10 [kV] and a frequency of 10 [kHz].	35
4.9	Voltage as a function of time for the three tested barrier materials. Discharge pulse initiated by a 10 [kV] voltage pulse.	36
4.10	Interpolation of the disturbed density area for the results of an ns-DBD plasma actuator with Kapton barrier fed with a burst of 100 pulses at 10 [kV] and 10 [kHz].	37
5.1	Schematic representation of the streamwise positioning of the covered HV electrode. Different scaling is used for x- and y-direction for better clarity.	43
5.2	The non-dimensional u-velocity boundary layer profile both at $U_\infty = 5$ [m/s] and 10 [m/s], with the flat surface of the model parallel to the freestream.	43
5.3	Disturbance growth in u-velocity difference (u') for both up and downstream position of the covered HV electrode in a laminar boundary layer with a 5 [m/s] freestream. Results acquired 0 [ms] after of a burst of 10 – 50 pulses of 10 [kV] at 10 [kHz].	44
5.4	Disturbance growth shown in contours of v-velocity difference (v'), with vector components (V') in both up and downstream position of the covered HV electrode. Disturbance in a laminar boundary layer with a 5 [m/s] freestream. Results acquired 0 [ms] after of a burst of 10 – 50 pulses of 10 [kV] at 10 [kHz].	45

5.5	Maximum absolute u-velocity (u') disturbance introduced by the ns-DBD plasma actuator in a laminar boundary layer with 5 [m/s] freestream. Values for upstream indicate a deceleration, those for downstream indicate an acceleration.	48
5.6	Disturbance in u-velocity difference (u') with vector components (V') for both up and downstream position of the covered HV electrode in a 5 [m/s] freestream. Results acquired 0 [ms] after of a burst of 50 pulses of 10 [kV] at 10 [kHz]. . . .	49
5.7	Disturbance in u-velocity difference (u') with vector components (V') for both up and downstream position of the covered HV electrode in a 10 [m/s] freestream. Results acquired 0 [ms] after of a burst of 50 pulses of 10 [kV] at 10 [kHz]. . . .	49
5.8	Voltage over time for the first pulse of a burst of 50 pulses at 10 [kV] and 10 [kHz] for the ns-DBD plasma actuator with the covered electrode in both streamwise positions.	51
5.9	Comparison of the validation data with the calculated density gradient in wall normal direction (synthetic Schlieren). Covered HV electrode in upstream position for both experiments, while the actuator is fed with a 10 [kV] signal at 10 [kHz]. Different scaling is used for x- and y-direction for better clarity.	53
5.10	Value of the incompressible continuity equation for the case with the covered HV electrode in upstream position with a 10 [kV] signal at 10 [kHz]. Different scaling is used for x- and y-direction for better clarity.	53
5.11	Perturbation with respect to the initial density field ($\rho_0 = 1.225 [kg/m^3]$) in percentages. Results for the measured flow field disturbances 0 [ms] after a burst of 10 – 50 pulses at 10 [kV] and 10 [kHz] for both upstream and downstream positioning of the HV covered electrode. Different scaling is used for x- and y-direction for better clarity.	54

List of Tables

3.1	Dimensional specifications of the ns-DBD plasma actuators tested in the Schlieren and PIV experiments.	15
4.1	Properties of the tested barrier materials.	26
4.2	Energy associated with the discharge of the tested ns-DBD plasma actuators. . .	37
5.1	Shape factor (H) of the boundary layer profiles shown in figure 5.2. Upstream and downstream correspond to the position of the covered HV electrode position of the ns-DBD plasma actuator.	43
5.2	Error in freestream u-velocity (u') between undisturbed and disturbed boundary layer flow at $y = 5.5 - 6.0$ [mm] from the wall.	47
5.3	Energy per pulse (E_{pp}) for the both upstream and downstream positioning of the covered HV electrode.	50

Nomenclature

Symbols

Symbol	Units	Description
<i>Latin symbols</i>		
A	$[m^2]$	Area.
C	$[F]$	Electrical capacity.
E_{in}	$[J]$	Energy input.
E_{out}	$[J]$	Energy output.
E_{pp}	$[J]$	Energy per pulse.
E/N	$[Td]$	Reduced Electric field strength.
H	$[-]$	Shape factor.
K_{sh}	$[-]$	Attenuation factor of the back-current shunt.
k	$[W/(m \cdot K)]$	Thermal conductivity.
l	$[mm]$	Actuator electrode length.
l_d	$[mm]$	Electrical zero-gap length.
R	$[\Omega]$	Electrical resistance.
R_{shunt}	$[\Omega]$	Resistance of the back-current shunt.
t_{bl}	$[mm/layer]$	Barrier thickness per layer of material.
t_b	$[mm]$	Barrier thickness.
t_e	$[mm]$	Electrode thickness.
u	$[m/s]$	Velocity component in x-direction.
u'	$[m/s]$	Velocity component in x-direction difference.
\vec{V}	$[m/s]$	Velocity vector.
$V_{actuator}$	$[V]$	Voltage applied over the actuator.
$V_{actuator}$	$[V]$	Voltage applied over the back-current shunt.
V'	$[m/s]$	Velocity field difference.
V_{dis}	$[m/s]$	Velocity field disturbed by plasma discharge.
V_0	$[m/s]$	Undisturbed velocity field.
v	$[m/s]$	Velocity component in y-direction.
v'	$[m/s]$	Velocity component in y-direction difference.
w_1	$[mm]$	Exposed electrode width.
w_2	$[mm]$	Covered electrode width.
w_b	$[mm]$	Barrier material width.
Z_{cable}	$[\Omega]$	Impedance.

Greek symbols

η_0	$[F/m]$	Absolute permittivity of vacuum.
η_r	$[-]$	Relative permittivity or dielectric constant.
μ	$[kg/(s \cdot m)]$	Dynamic viscosity.
μ_0	$[kg/(s \cdot m)]$	Reference dynamic viscosity.
ν	$[m^2/s]$	Kinematic viscosity, $\nu = \mu/\rho$
ρ	$[kg/m^3]$	Density.
ρ_{vr}	$[\Omega \cdot m]$	Electrical volume resistivity.

Acronyms

Acronym	Description
BTBS-FD	Backward-time backward-space finite difference.
FOV	Field Of View.
HV	High Voltage.
PIV	Particle Image Velocimetry.
RPM	Rotations Per Minute.
SOC	Sum of Correlation.
ac-DBD	Active current Dielectric Barrier Discharge.
ns-DBD	Nanosecond pulsed Dielectric Barrier Discharge.

Chapter 1

Introduction

Flow control and the physical mechanisms in which it is achieved has been of interest to aerodynamic studies for many decades [Gad-el Hak (2000)]. In recent years more research has been devoted to dielectric barrier discharge (DBD) plasma actuators, primarily due to their low weight, fast response time and low energy consumption [Moreau (2007), Corke et al. (2009)]. The two main types of DBD plasma actuator historically investigated are geometrically identical but their voltage driving signal and working principles are different. The first type, an ac-DBD plasma actuator, is driven by an alternating current (ac) signal, which imposes electrohydrodynamic (EHD) forces on the near wall volume of air [Enloe et al. (2004a), Enloe et al. (2004b)]. Experimental and numerical works have shown that the body force is able to induce a momentum flow with a maximum value of about 8 [m/s] [Moreau (2007), Corke et al. (2009)]. The other main type, an ns-DBD plasma actuator, is driven by a pulsed voltage signal with very short rise and decay times and a pulse width of tenths of nanoseconds. This dissociates the air particles and excites their translational degrees of freedom [Berdushev (1988)], which lead to a rapid local increase in temperature [Boeuf and Kunhardt (1986), Nagaraja and Yang (2013)]. It has been shown that an ns-DBD plasma actuator is able to excite instabilities in a bounded or free shear layer [Correale et al. (2014)], which can lead to spanwise vortex roll-up [Gaitonde et al. (2013)]. Focus in this thesis is on the ns-DBD plasma actuator and the associated thermal effect.

Experimental investigations on ns-DBD plasma actuators revealed that local flow effects are a small body force [Roupassov et al. (2009), Little et al. (2012)], a weak compression wave [Roupassov et al. (2009), Little et al. (2012), Benard et al. (2012)], and an overheating in the discharge region [Roupassov et al. (2009), Little et al. (2012), Correale et al. (2014)]. According to Little et al. (2012), the small body force is capable of an induced velocity of 0.5 [m/s], which is much smaller compared to the 8 [m/s] of an ac-DBD plasma actuator. The weak shock wave is considered to have very little effect on a bounded or free shear layer [Popov and Hulshoff (2012), Zheng et al. (2014)]. Roupassov et al. (2009) hypothesized that the main mechanism of impact for this actuator is the energy transfer to and the heating of the near-surface gas layer. However, this energy transfer and the coupling to the local

flow instabilities still needs to be investigated further. Moreover, [Michelis et al. \(2013\)](#) and [Correale et al. \(2014\)](#) have shown by means of Schlieren images that each pulse thermalises a small amount of air in the discharge volume. This increases the local air temperature and affects the local density and viscosity. Quantification of these local density fields is primarily achieved by determining the increase in local temperature by either energy input determination [[Roupassov et al. \(2009\)](#)] or by modeling the plasma kinetics [[Takashima et al. \(2013\)](#)]. Experimental Schlieren images are then used to validate a numerical simulation which uses the approximated temperature as boundary condition, such to approximate the quantitative density field [[Opaits et al. \(2008\)](#)].

Studies on ac-DBD plasma actuators, by for instance [Forte et al. \(2007\)](#), have shown that the barrier should have a low dielectric constant, a high dielectric strength and a large thickness to produce a large body force. However, as of now, a characterization study on the influence of the barrier in ns-DBD plasma actuators on the resulting flow effects has not yet been conducted.

Fundamental understanding of the working principles of an ns-DBD plasma actuator is of importance for the improvement of the technology. With a prospect to eventually use it outside of a controlled lab environment.

The aim of this study is to uncover the influence of the barrier material on the thermal energy deposition of an ns-DBD plasma actuator. In a addition, a study in the local flow effects of discharge by an ns-DBD plasma actuator in a laminar boundary layer is performed. Chosen barrier materials for this study are Kapton[®] Polyimide tape, silicone-rubber, and Fine Polyamide PA2200. The thermal energy deposition effects to the nearby air of these barriers have been investigated with the use of Schlieren imagery in quiescent conditions. Next to this, electrical energy measurements are made with the back-current shunt technique. Discharge characterization on both structure and intensity has been performed with direct imaging of the discharge. Additionally, the effect of a flush mounted ns-DBD plasma actuator with a barrier of consisting of 2 layers Kapton tape on a low velocity laminar boundary layer is investigated with the use of phase-locked planar Particle Image Velocimetry (PIV). From the velocity fields the local density field is calculated with a backward-time backward-space finite difference discretization of the compressible continuity equation. This method is validated with experimental Schlieren data.

This thesis report consists of a theoretical and experimental background study in chapter 2, followed by the description of the Experimental Setup in chapter 3. The results of the study into the influence of the barrier on the tested ns-DBD plasma actuators are presented in chapter 4. The effect of discharge by ns-DBD plasma actuator on a laminar boundary layer and the quantification of the density changes is shown in chapter 5. Chapter 6 contains the final conclusions and recommendations of this report, followed by the bibliography.

Chapter 2

Background

Usage of nanosecond pulsed dielectric barrier discharge (ns-DBD) plasma actuators for flow control purposes and research into its working principles is studied by academia for the past few decades. In order to have a better understanding of the previous and current research, the fundamental principles of these actuators will be discussed first. However, recently it has been shown by [Michelis et al. \(2013\)](#) and [Correale et al. \(2014\)](#) that the ns-DBD plasma actuators mostly rely on the thermal energy deposition in the boundary layer. As a result, a specific part of the literature research is devoted to near wall temperature effects on the boundary layer by devices other than plasma actuators.

This chapter contains both boundary layer theory and relevant experimental results from other authors in the fields of both plasma actuators and thermalization of boundary layers.

2.1 Boundary layer theory

The ns-DBD plasma actuator affects the boundary layer that is formed over it. In order to have a better understanding of the flow effects of these actuators, the boundary layer theory needs to be discussed first. This theory is a simplification of the full Navier-Stokes equations. The incompressible momentum equation at a wall, with a no-slip condition, without body forces and assumed on a wall with almost no curvature can be simplified to equation 2.1. Here density (ρ), pressure (p) and wall tangential velocity (u) gradients are related to the wall normal velocity (v_w) and local dynamic viscosity (μ) gradient.

This equation shows that an adverse pressure gradient ($\frac{\partial p}{\partial x} > 0$), without viscosity gradients and wall normal velocity, will create an inflection point in the velocity profile. This means

that the flow is decelerated close to the wall, possibly to the point of separation.

$$\rho v_w \frac{\partial u}{\partial y} \Big|_{y=0} + \frac{\partial p}{\partial x} \Big|_{y=0} - \frac{\partial \mu}{\partial y} \Big|_{y=0} \frac{\partial u}{\partial y} \Big|_{y=0} = \mu \frac{\partial^2 u}{\partial y^2} \Big|_{y=0} \quad (2.1)$$

By assuming there is no wall normal velocity ($v_w = 0$) and zero pressure gradient ($\frac{\partial p}{\partial x} = 0$), only the relation between velocity and viscosity remains as shown in equation 2.2. In order to relate this to the local temperature (T) the Sutherland equation is used as described by [White \(2006\)](#) and shown in equation 2.3. In this equation the Sutherland constant (S), is used to relate the reference conditions (μ_0 and T_0) to the actual conditions (μ and T). It can be shown that the dynamic viscosity increases with temperature in gasses, and decreases with temperature in liquids. Dynamic viscosity will always increase with pressure in gas.

$$\frac{\partial^2 u}{\partial y^2} \Big|_{y=0} = -\frac{1}{\mu_{y=0}} \frac{\partial \mu}{\partial y} \Big|_{y=0} \frac{\partial u}{\partial y} \Big|_{y=0} \quad (2.2)$$

$$\frac{\mu}{\mu_0} \approx \left(\frac{T}{T_0} \right)^{3/2} \frac{T_0 + S}{T + S} \quad (2.3)$$

With the assumption that in initial condition the velocity gradient at the wall is positive ($\frac{\partial u}{\partial y} \Big|_{y=0} > 0$), two cases can be defined based on equations 2.2 and 2.3:

- Wall temperature is higher than the medium above it ($T_{y=0} > T_{y>0}$). This negative temperature gradient normal to the wall is proportional to the dynamic viscosity gradient at the wall in case of a gaseous medium. This implies an inflection point will exist in the velocity profile curvature, destabilizing the boundary layer. The inverse is true for a liquid boundary layer.
- Wall temperature is lower than the medium above it ($T_{y=0} < T_{y>0}$). This positive temperature gradient normal to the wall is proportional to the dynamic viscosity gradient at the wall in case of a gaseous medium. This implies a more negative velocity profile curvature, leading to a fuller velocity profile and a more stabilized boundary layer. The inverse is true for a liquid boundary layer.

2.2 Dielectric Barrier Discharge actuators

Recently the topic of interest in aerodynamic flow control studies has shifted to flow control by dielectric barrier discharge (DBD) plasma actuators. The DBD has advantages with regard to other flow control devices because it is a flow control device of low mass which can be mounted flush to a surface, which consumes low amounts of energy and has a fast response

time [Moreau (2007), Corke et al. (2009)]. The two main types of DBD plasma actuators can be geometrically identical, but are very different in their voltage driving signal and flow control mechanisms.

For example, the ac-DBD plasma actuator is driven by a sinusoidal high voltage (active) current and affects the flow locally by electro-hydrodynamic forces, effectively creating a body force. Optimizations by Forte et al. (2007) showed that a momentum jet can be induced with a velocity of about 8 [m/s].

In contrast, the ns-DBD plasma actuator is driven by a pulsed high voltage signal with very short rise and decay times and a pulse width of typically tenths of nanoseconds. The short rise and decay times of this high voltage pulse dissociates the air particles and excites their translational degrees of freedom [Berdushev (1988)], which lead to a rapid local increase in temperature [Boeuf and Kunhardt (1986), Nagaraja and Yang (2013)]. Experiments have shown that this actuator locally affects the near wall air with a small body force [Roupassov et al. (2009), Little et al. (2012)], a weak compression wave [Roupassov et al. (2009), Little et al. (2012), Benard et al. (2012)] and an overheating in the discharge region [Roupassov et al. (2009), Little et al. (2012), Correale et al. (2014)]. Additionally, Correale et al. (2011) showed leading edge separation control leading to lift force increase for Reynolds numbers up to $3 \cdot 10^6$ [–].

2.2.1 ns-DBD plasma actuator

An ns-DBD plasma actuator consists of two non-overlapping electrodes separated by a (dielectric) barrier material. This is schematically shown in figure 2.1. The rising absolute voltage of the nanosecond pulsed signal increases the high reduced electric field (E/N) between the electrodes above the breakdown value, which is the value that is needed to generate electron-ion pairs through electron impact ionization of the neutral gas. This breakdown generates a low temperature plasma [Kunhardt (1980), Kunhardt (2000)] in which electrons or positive ions are deposited on the dielectric surface. This process is visible through streamers and filaments. When the absolute voltage rapidly decays, the difference in potential between the charged surface and the electrodes initiates the reverse reaction, with the filaments showing more branching [Benard et al. (2012)]. The created high reduced electric field strength (E/N) of 1000 [Td] (as determined by Aleksandrov et al. (2010)), results in quenching in the electrochemical reactions which is capable of high initial background gas heating according to Boeuf and Kunhardt (1986) and Nagaraja and Yang (2013).

Nanosecond pulsed dielectric barrier discharge (ns-DBD) plasma actuators are shown to be effective in high speed laminar leading edge separation control. Results by Rethmel et al. (2011) and Little et al. (2012) indicate that the stall angle of attack can be increased by a few degrees at Reynolds numbers of $1.6 \cdot 10^6$ [–]. Work within the own department by Correale et al. (2011) on a Natural Laminar Flow airfoil with Reynolds numbers up to $3.2 \cdot 10^6$ [–] showed that airfoil performance increased at high numbers of attack with a low amount of actuation power.

The main mechanism of impact of these actuators was hypothesized by Roupasov et al. (2009) to be the energy transfer to and heating of the near-surface gas layer. The resulting flow effects induce a momentum transfer into the boundary layer, which improves the attachment of the boundary layer. Conclusions of Rethmel et al. (2011) and Little et al. (2012) are that at high Reynolds numbers the ns-DBD functions as an active trip at pre-stall angles of attack and provides perturbations that generate coherent spanwise vortices at post-stall angles. Large Eddy Simulations (LES) by Gaitonde et al. (2013) showed that a shear layer which separates from a leading edge can be tripped by a ns-DBD plasma actuator. This leads to spanwise vortex roll-up which is followed by reattachment of the turbulent boundary layer to the airfoils surface.

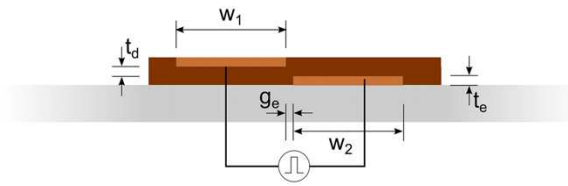


Figure 2.1: Schematic representation of a DBD plasma actuator in side view. Indicated are the electrode widths (w_1 , w_2), electrode thickness (t_e), barrier thickness (t_d) and inter electrode gap (g_e) [Correale et al. (2014)].

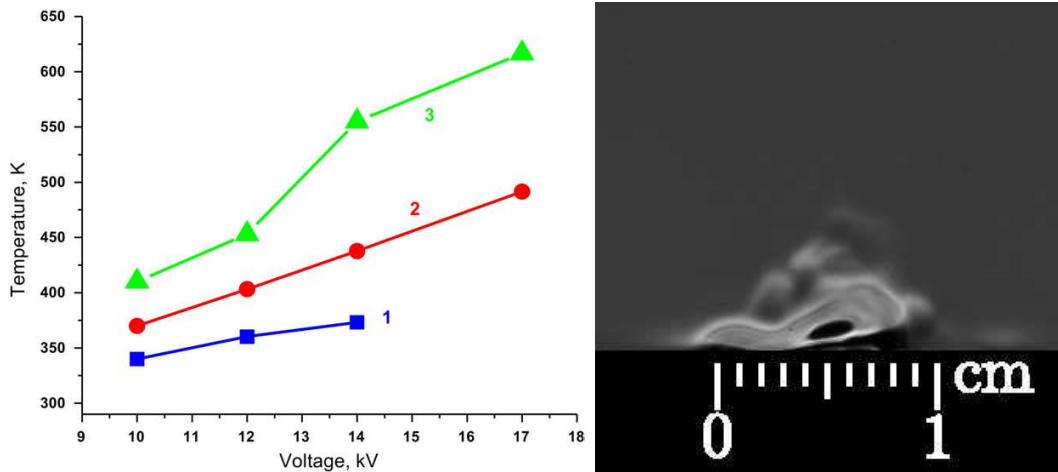
Thermal energy deposition

The high reduced electric fields (E/N) of 1000 [Td] at which the ns-DBD plasma actuators operate [Aleksandrov et al. (2010)] causes a high fraction of the total energy to go quickly into gas heating. This is a result of the more efficient excitation of the electron degrees of freedom, dissociation and ionization processes that take place at this field strength. The energy release during molecular dissociations and ionization by electrode impact is a governing process in fast gas heating as shown by Berdushev (1988) and Nagaraja and Yang (2013). Next to this, Boeuf and Kunhardt (1986) and Popov (2001) showed that the high velocity of propagation of the plasma discharge is only possible due to the high local heating of $3 \cdot 10^9$ [K/s] at the streamer heads.

Roupasov et al. (2009) indicated that with pulse durations of 7, 12 and 50 [ns], the temperature in the plasma layer can reach values of 70, 200 and 400 [K] respectively. The dependency of temperature in the plasma layer on the applied voltage was shown by Aleksandrov et al. (2010) in figure 2.2(a). Experiments of Roupasov et al. (2009) and Aleksandrov et al. (2010) showed that at high reduced electric field and atmospheric pressure the energy efficiency in convergence from electricity to heat through ns-DBD plasma actuators is about 56 – 66 %. The pressure in the plasma rises by 1 [atm] when an energy input of 4.5 [mJ/cm] was given according to Starikovskii et al. (2009). In addition, studies by Michelis et al. (2013) and Correale et al. (2014) demonstrate with Schlieren experiments that each discharge pulse thermalizes a certain amount of air, resulting in a density change which can be visualized by Schlieren. This is shown in figure 2.2(b). The growth of the volume of thermalized air was determined to be most linear with energy input, hence linear with amount of pulses. They also showed that in a laminar boundary layer the velocity disturbance

downstream of the actuator grows within the boundary layer itself unless it breaks down to a turbulent spot.

Density field disturbances are usually shown by means of qualitative Schlieren imagery. However, a few studies used a Navier-Stokes solver coupled with a plasma kinetics model or a simulated temperature hot-spot to approximate density and temperature fields associated with ns-DBD discharge. [Unfer and Boeuf \(2009\)](#) recreated experiments by [Starikovskii et al. \(2009\)](#) numerically to calculate the temperature field. [Zhu et al. \(2013\)](#) and [Zheng et al. \(2014\)](#) used a plasma kinetics model to recreate experimentally the energy and electron temperature data. From this follows a density and air temperature field. They conclude that locally the air is heated to about 1170 [K]. However, this maximum instantaneous value is much higher the temperatures measured in experiments by [Roupassov et al. \(2009\)](#).



(a) Gas temperature in the plasma layer; immediately after discharge (1), 1 $[\mu s]$ after discharge (2), calculation under perfect conditions (3)[[Aleksandrov et al. \(2010\)](#)].

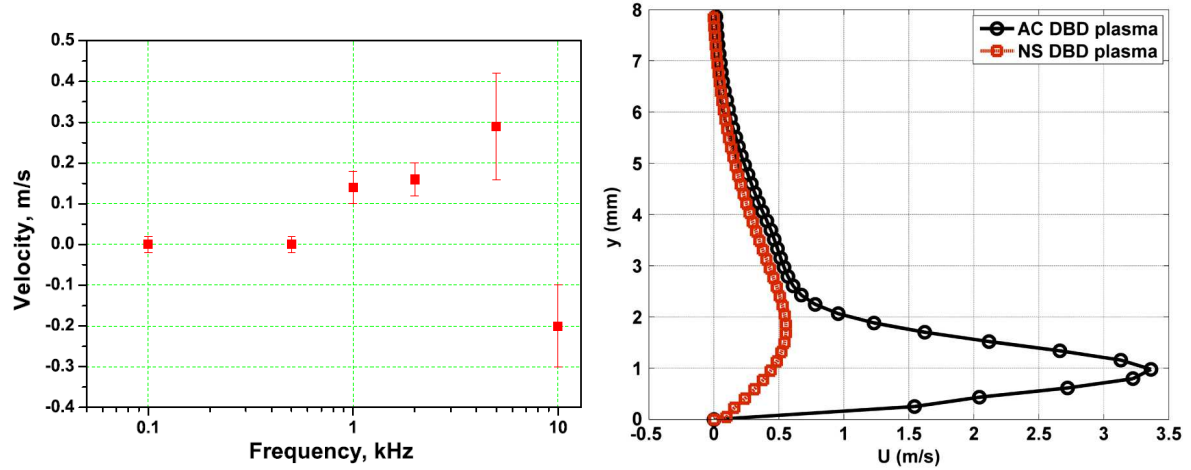
(b) Heated volume visualized by Schlieren, 6 $[ms]$ after the start of a burst of 50 pulses at 10 $[kHz]$ and 10 $[kV]$ [[Michelis et al. \(2013\)](#)].

Figure 2.2: Thermal energy deposition effect by ns-DBD plasma actuator.

Body force

Experimental studies by [Roupassov et al. \(2009\)](#) and [Little et al. \(2012\)](#) indicate that the momentum jet magnitude induced in the flow is much lower for ns-DBD than for ac-DBD plasma actuators. This is shown in figure 2.3. [Little et al. \(2012\)](#) reported a induced velocity of 0.5 $[m/s]$ for ns-DBD plasma actuators, while [Roupassov et al. \(2009\)](#) reported absolute values no larger than 0.3 $[m/s]$. Moreover, flow field visualizations by [Zhu et al. \(2013\)](#) and [Wu et al. \(2014\)](#) show that a positive vertical velocity component is created by the heated up volume of the quiescent air above an actuator. The associated small body force is 15 $[mN]$ in vertical and almost zero force in horizontal direction. At high speed and high Reynolds numbers flow instabilities are high and background noise is dominant, this is why [Kim et al. \(2010\)](#) summarized that actuators need to have both high bandwidth and high amplitude to

be effective for high speed flow control. This implies that a small body force is probably not the primary flow control mechanism of an ns-DBD plasma actuator at high Reynolds number tests.



(a) Pulse length 25 [ns], rise time 8 [kHz] and a pulse amplitude of 20 [kV] [Roupassov et al. (2009)].

(b) 20 [mm] Downstream of an ns- and ac-DBD plasma actuator at 2[kHz] and 30[kV] [Little et al. (2012)].

Figure 2.3: Induced velocities for ns-DBD plasma actuators.

Weak compression wave

Observations in both numerical and experimental studies show the formation of weak shock waves emanating from the discharge area. Studies by Starikovskii et al. (2009) and Benard et al. (2012) showed that a spherical weak shock wave is formed by each streamer in the discharge. This shock wave is caused by the rapid heating of gas at the head of the streamer. When viewed along the electrodes a single cylindrical shock wave is visible, centered at the edge of the exposed electrode as shown by Benard et al. (2012). A single high voltage pulse consists of two discharge phases. Therefore, two shock waves are formed rapidly after each other, as demonstrated by Benard et al. (2012) in figure 2.4. The velocity of this weak shock wave is slightly above the speed of sound at initiation, but decreases to the speed of sound in 4 – 5 [μ s] after initiation [Roupassov et al. (2009)]. However, as hypothesized by Popov and Hulshoff (2012) and Zheng et al. (2014) these weak shock waves have little effect on a shear layer.

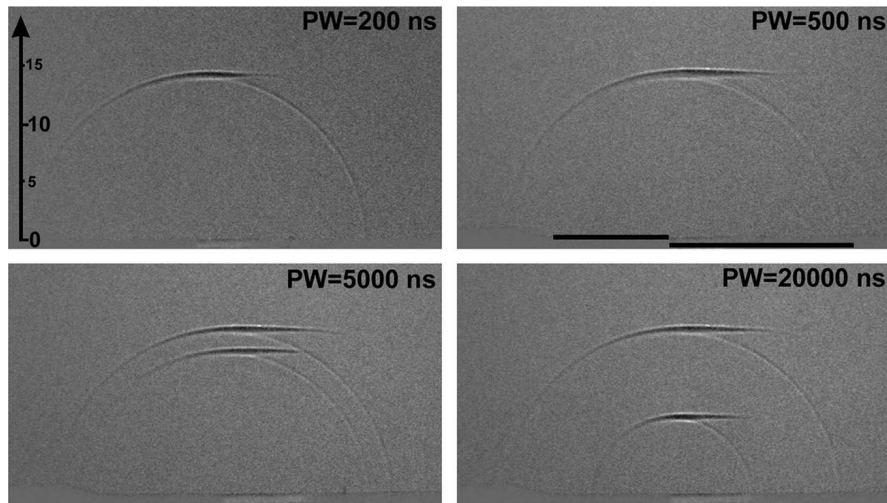


Figure 2.4: Induced shock wave 10 [μs] after discharge at +10 [kV]. Scale in mm , with indicated pulse width (PW) [Benard et al. (2012)].

2.2.2 Barrier materials

The electric characteristics and thickness of the barrier in a DBD plasma actuator have a pronounced effect on the discharge behavior because it is the only material separating the two electrodes.

Studies covering ac-DBD plasma actuators indicate that a thick barrier with low dielectric constant is able to produce a larger body force better than a thin barrier with a high dielectric constant [Corke et al. (2010), Cattafesta and Sheplak (2011) and Forte et al. (2007)]. Hence, for body force production a PMMA (Plexiglas) barrier is better for body force generation than a Kapton barrier. Moreover, Forte et al. (2007) made a direct comparison between two barrier materials (PMMA and glass) and he reached the same conclusion. Charge accumulation on the barrier surface is a limitation in the production of body force by ac-DBD plasma actuators as recognized by Opaitis et al. (2008). Results showed that it can be partially removed with conductive coatings, which makes the barrier capable of sustaining charge build up for longer.

With regard to barrier materials, the ns-DBD plasma actuators have not been extensively investigated, with the most common barrier material being Kapton tape. This is used by multiple authors such as Roupasov et al. (2009), Little et al. (2012), Correale et al. (2014). Kapton tape has a high dielectric constant and breakdown voltage and has a low thickness, making it in tape-form easy to use for experiments. A high reduced electric field can be created between the electrodes due to the small distance between the electrodes, essential for ns-DBD operation. However, only one study specifically on ns-DBD plasma actuator barriers was found. This study by Aba'a Ndong et al. (2013) indicates that polyimide type barriers (such as Kapton) when used at high frequencies will degrade by temperature, electric field and radiation resulting in less efficient coupling of energy to the air.

2.3 Boundary layer thermalization effects by non-plasma actuation.

Experimental equivalence of the boundary layer theory stated in section 2.1 is sought in this section. The difference in wall temperature control and volumetric temperature control will be shown by means other than DBD plasma actuators. Also experiments on phase control are discussed.

2.3.1 Wall temperature control

The opposite reaction of flow in liquid and gasses to wall heating of a cylinder suggests that flow control through wall heating is caused by changes in both density, but primarily, dynamic viscosity according to [Lecordier et al. \(2000\)](#). The heating of the cylinder surface in air reduces the vortex shedding due to a more turbulent boundary layer. This destabilization of the boundary layer in airflow by wall heating is also shown by an experiment of [Reed and Saric \(2013\)](#) on swept wings. They showed that heating of the attachment line on a swept wing in compressible flow of Mach 0.8 causes the boundary layer to become fully turbulent over the entire wing.

In flight tests by [Dougherty and Fisher \(1980\)](#) it was shown that with wall cooling the Reynolds number of a cone varied with a factor T_w^{-7} , meaning a boundary layer can be kept laminar for longer, reducing skin friction.

Phase control can be used to promote or delay transition in the boundary layer. Out-of-phase (relative to the local/natural instabilities) pulsed local spanwise wall heating was used to damp instability waves in a boundary layer, while in-phase pulses excited the boundary layer in experiments by [Liepmann and Nosenchuck \(1982\)](#). The local instabilities were measured by the shear-stress fluctuation. The increase in transition Reynolds number was achieved with only 10 [W] of electric power.

2.3.2 Volumetric temperature control

Volume supply of energy to a boundary layer above a thermally insulated plate shows a decrease in the growth of unstable perturbations, even at large distances from the heat source [Kazakov and Kogan \(1988\)](#). This is because the boundary layer then behaves as a flow with smaller Reynolds number.

Numerical experiments by [Levin and Larin \(2003\)](#) indicate that a turbulent boundary layer with a submerged heat addition region causes a friction force reduction up until a certain optimum of heat addition. More heating only results in more intense heat fluxes at the wall.

Local Arc Filament Plasma Actuators (LAFPAs) and ns-DBD plasma actuators are similar

in the way that flow control is archived by rapid localized heating. The arc filament between two electrodes creates temperatures over $1000 [^{\circ}C]$. The associated local pressure and volume rise excites the natural flow instabilities when in phase with these instabilities. These local pressure perturbations are hypothesized to act as a solid obstacle suddenly placed in the flow by Samimy et al. (2004) and Kim et al. (2010).

2.4 Discussion

A few conclusions can be drawn from the literature summarized in this chapter:

- An ns-DBD produces locally a small body force, a fast thermal energy deposition and a weak shockwave. As a result, these local effects are capable of exciting the natural flow instabilities in order to trip a laminar boundary layer and produce coherent spanwise vortices in a separated shear layer.
- The body force produced by ns-DBD plasma actuators is much smaller than that of a ac-DBD plasma actuator. It is therefore considered to have only limited contribution to the flow control capabilities of a ns-DBD a high Reynolds number flows.
- The weak compression wave was shown by Popov and Hulshoff (2012) and Zheng et al. (2014) to have limited effect on excitement of a shear layer. This is why in this study the weak shock waves are not considered as flow control device.
- Fast thermalization of the near wall volume by ns-DBD as shown by Correale et al. (2014) does not produce the stabilization effect on the air as suggested in theory by White (2006) and experiments by Kazakov and Kogan (1988). This may prove that a ns-DBD plasma actuator acts more through the pulsed wall heating, which has been shown to turbulise a boundary layer in experiments by Liepmann and Nosenchuck (1982).
- Apart from numerical simulations no experimental data of the local direct effect of density and viscosity changes by ns-DBD plasma actuation on a boundary layer has been determined. This while the origin of these changes through temperature is accredited with the mechanism through which a ns-DBD plasma actuator achieves flow control.
- The effect of the barrier used for DBD plasma actuators has only been investigated on ac-DBD plasma actuators. For ns-DBD plasma actuators the most common barrier material is Kapton, because of its low thickness and high dielectric strength.

The research questions that are asked at the beginning of this investigation are therefore:

- What is the influence of different barrier materials on the thermal deposition by the discharge of a ns-DBD plasma actuator?
- What is the direct effect of the local energy addition by an ns-DBD plasma actuator on a laminar boundary, such that natural flow instabilities are excited?

Chapter 3

Experimental setup

This chapter gives an overview of the experimental apparatus and geometric specifications used in both the barrier characterization study and the laminar boundary layer experiment. The construction of the tested ns-DBD plasma actuators (section 3.1), specification of the Schlieren and discharge image acquisition setups (sections 3.2 and 3.3) are followed by the description of the wind tunnel facility and wind tunnel model (sections 3.4 and 3.5). The specifications of the Particle Image Velocimetry (PIV) experiment are presented in section 3.6. The energy measurements are explained in section 3.7, followed by the barrier characterization tests in section 3.8.

3.1 ns-DBD plasma actuator

The tested ns-DBD plasma actuators consist of two non-overlapping adhesive copper tape electrodes separated by a barrier material. The horizontal gap between the adjacent edges of the electrodes is approximately zero. A schematic representation viewed along the electrode length of the actuator with a barrier made out of 2 layers of Kapton tape, is shown in figure 3.1. A top view is shown in figure 3.2. The dimensions of the tested actuator and the barrier specifications are shown in table 3.1. The three barrier materials selected are:

- Kapton[®] Polyimide tape (hereafter called Kapton). This is chosen because of its high dielectric strength and low thickness. It is used in many experiments on ns-DBD plasma actuators.
- Silicone-rubber (hereafter called silicone). This is chosen because of its presumed lower dielectric strength and its more resistive qualities than Kapton. It is tested in 1.5, 2 and 3 [mm] thickness.
- Fine Polyamide PA2200 (hereafter called PA2200). This is a material used in powder form in laser sintering and 3D printing. These processes result in a solid yet porous structure, as visible in the tested barriers. The material itself is a plastic (and therefore

dielectric), but the porous structure can alter the electrical properties of the barrier. These tested barriers have a thickness of 1, 2 and 4 [mm].

The Kapton based ns-DBD plasma actuator is constructed by taping the covered copper electrode to the plastic substrate used as support. On top of this the various layers of Kapton are taped before the exposed copper electrode is taped on top of the Kapton tape. For this experiment the Kapton tape layers are carefully stuck on top of each other in order to avoid the formation of air bubbles between the separate layers. In case of the Silicone-rubber and PA2200 barriers both copper electrodes are taped to the barrier material before fixing it to the support substrate with tape.

The actuator is connected with a high voltage coaxial cable (type RG-217) of $50[\Omega]$ impedance and $20[m]$ long to a power generator. In the present investigation the covered electrode is always connected to the high voltage output of the power generator, with the exposed electrode connected to ground potential. The discharge of all the different actuators tested is driven by a FID Technologies fast solid state power generator which provides a $12.5[kV]$ nominal pulse voltage and about $10[kV]$ applied voltage. This voltage is applied with a pulse rise and decay time of about $3[ns]$ and a fixed pulse width of $23[ns]$ (measured between 10 – 90% of maximum voltage). The timing of the trigger, frequency and amount of pulses per discharge burst is controlled through a Tektronics AFG3252 Arbitrary Function Generator connected to the external trigger input of the power generator. For the Schlieren imagery, discharge characterization and energy measurements the ns-DBD plasma actuators are situated in a transparent still air box.

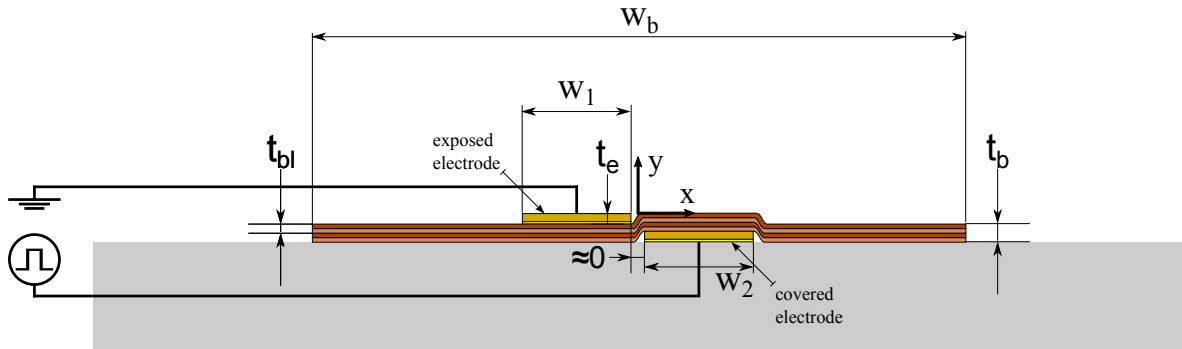


Figure 3.1: Schematic representation of an ns-DBD plasma actuator, viewed along the electrodes. Different scaling is used for x- and y-direction for better clarity.

Next to the experiments in a still air box, also experiments with the ns-DBD plasma actuator situated in a boundary layer flow are conducted. Figure 3.3 shows schematically the ns-DBD plasma actuator flush mounted in the groove of the used boundary layer model. The tested actuator for the boundary layer tests has a barrier made out of 2 layers of Kapton tape of $20[mm]$ wide. The total length for discharge is approximately $300[mm]$ long. The Kapton and electrode dimensions and specification are otherwise equal those in the still air experiments. This actuator is constructed by connecting the two adhesive sides of the Kapton tape together, with the electrodes mounted on either side. The horizontal gap between the

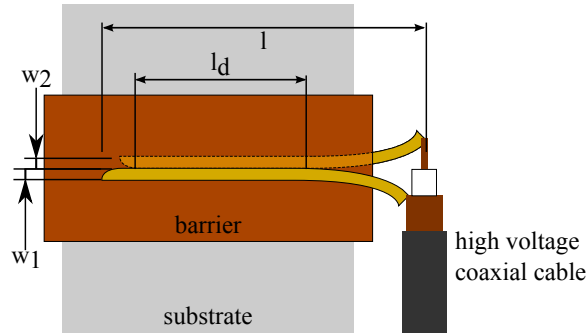


Figure 3.2: Schematic representation of an ns-DBD plasma actuator, shown in top view.

Table 3.1: Dimensional specifications of the ns-DBD plasma actuators tested in the Schlieren and PIV experiments.

Symbol	Description	Material		
		Kapton	Silicone	PA2200
w_1	Exposed electrode width [mm]	5	5	5
w_2	Covered electrode width [mm]	5	5	5
w_b	Barrier material width [mm]	50	50-75	75
w_g	Barrier/Groove width [mm]	20	-	-
t_{bl}	Barrier thickness [mm/layer]	0.089	1.5, 2, 3	1, 2, 4
t_b	Barrier thickness [mm]	0.178, 0.356, 0.534	1.5, 2, 3	1, 2, 4
t_e	Electrode thickness [mm]	0.1	0.1	0.1
l	Actuator electrode length [mm]	140	140	140
l_d	Electrical zero-gap length [mm]	90	90	90

edges of these electrodes is approximately zero and is called the 'zero-gap line'. For better flush mounting extra Kapton tape is used to fill gaps in the groove. This complete actuator is fixed to the groove of the model with spray-on glue that allowed remounting. This ensures that the streamwise position of the electrodes with respect to each other can be parameterized without changing the electrical specifications of the actuator. Also in this experiment the covered electrode is connected to the high voltage output of the power generator, while the exposed electrode is grounded.

The electrodes of the ns-DBD plasma actuator are connected to the high voltage coaxial cable (type RG-127) downstream of the model, such to avoid blockage by this high voltage cable in the measurement area. This connection consists of a pair of two copper-tape electrodes separated by 6 layers of Kapton tape on either side of the flat surface of the model for symmetry. This is visible in figure 3.8.

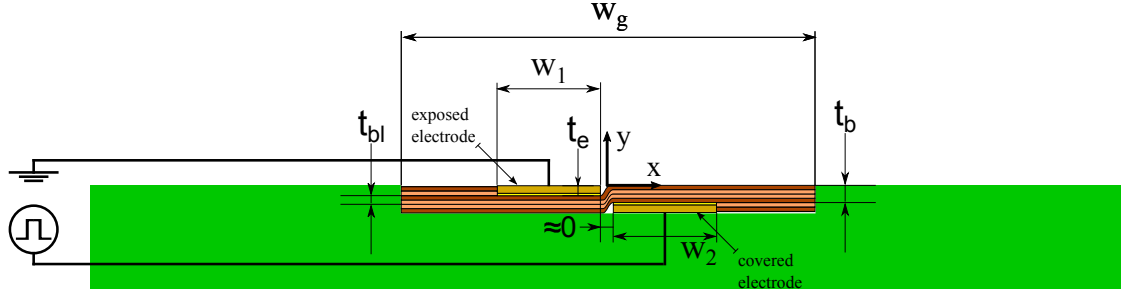


Figure 3.3: Schematic representation of an ns-DBD plasma actuator in the groove of the boundary layer model in the W-tunnel. Displayed configuration shows the covered high voltage electrode in downstream streamwise position. Different scaling is used for x- and y-direction for better clarity.

3.2 Schlieren imagery

The Schlieren experiment is conducted with a typical Z-setup as described by Settles (2001). An extra mirror is used to conduct the experiment in the available space, as shown in figure 3.4.

Time resolved images are taken with a La Vision Images pro HS 4M camera which carries a 12 bit CCD sensor with $2016 \text{ pixels} \times 2016 \text{ pixels}$, totaling to 4 Megapixels. Full frame measurements are acquired at a 1 [kHz] acquisition frequency and an exposure time of between 2 and $5 \text{ [}\mu\text{s]}$. This variation was caused by the setup location, which required a new calibration each day. This resulted in different light intensities and system density gradient sensitivity.

A continuous light source of 50 [W] is provided by a beamer Arc lamp (SolarcTM Lighting Technology). Two equal parabolic mirrors with a focal distance of 1.5 [m] are used with 3 spherical lenses to form the collimated light beam needed for Schlieren. The Field of View (FOV) is $110 \text{ [mm]} \times 110 \text{ [mm]}$ which results in a image magnification (M) of 0.2 [-] . The knife edge is set such that the density gradient is visualized perpendicular to the surface of the ns-DBD plasma actuator. The system of the camera with the power generator and ns-DBD plasma actuator is synchronized with the use of the AFG3252 Arbitrary Function Generator.

The tested ns-DBD plasma actuators are situated within a still air box made out of transparent Plexiglas with a size of $500 \text{ [mm]} \times 500 \text{ [mm]} \times 1000 \text{ [mm]}$. The origin of the dimensional field was set at the zero-gap edge of the exposed electrode on the surface of the barrier material. The exposed electrode is always in positive x-location, between 0 and 5 [mm] . The plasma discharge consists of a single burst of pulses at a frequency of 10 [kHz] . The amount of discharge pulses in each burst varies from 10 to 1000 pulses, with a minimal image acquisition time of 100 [ms] . This acquisition time is increased to 150 [ms] when more than 500 pulses are applied, such to capture the density gradient field after discharge for at least 50 [ms] .

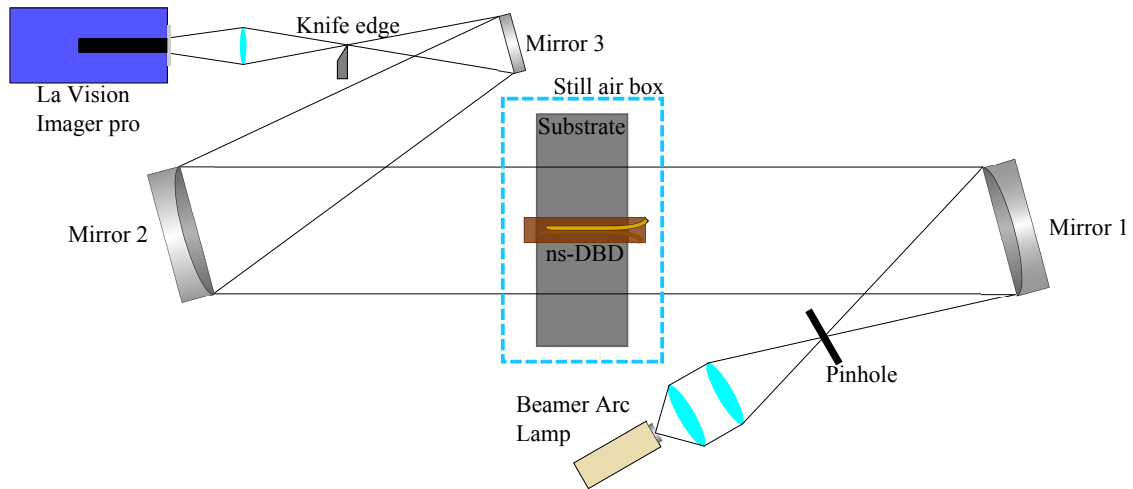


Figure 3.4: Schematic representation of the z-type Schlieren set-up.

3.3 Discharge characterization

The light intensity and filamentary state of the discharge on the different barriers was photographed with the use of a Nikon D80 camera with CCD sensor of 10.2 Megapixel ($2872 \text{ pixels} \times 2592 \text{ pixels}$). As shown in figure 3.5, this camera looked down onto the actuator which was situated in the still air box. The Field of View (FOV) was $460 \times 310 [mm]$, corresponding to a magnification of $0.05 [-]$. The camera was set to a sensitivity of $ISO 400$ and a diaphragm f-stop of 3.8 . The discharge was initiated before, and ended after, the image acquisition. This image was acquired with an exposure time of $1 [s]$, meaning that discharge duration was longer than $1 [s]$. To ensure only discharge associated light was used in the calculations, a background image was taken before each discharge image and subtracted of that discharge image. Next to this the still air box and connection to the lens were wrapped in black cloth such to block the surrounding light as much as possible.

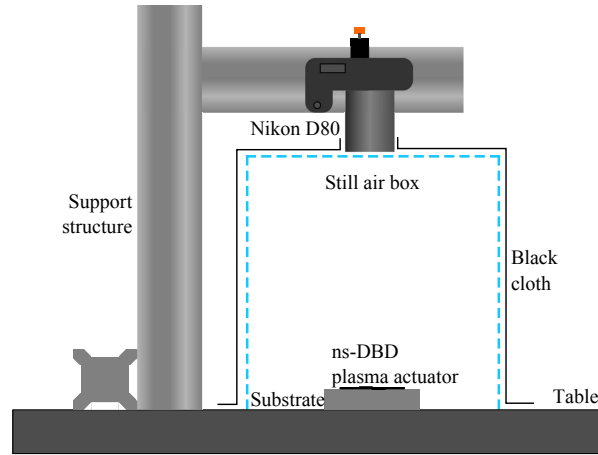


Figure 3.5: Schematic representation of the setup for discharge imaging.

3.4 Wind tunnel facility

The experiments are conducted in the W-tunnel of the Aerodynamics department of the faculty of Aerospace Engineering. This tunnel is configured such that it has a Plexiglas closed test section of $400 [mm] \times 400 [mm] \times 600 [mm]$ with an open exit. It is capable of a maximum velocity of $40 [m/s]$ with a turbulent intensity of approximately 0.1% at this maximum velocity. The room in which the tunnel is situated is equipped with an external air extraction system, capable of removing PIV tracer particles.

The velocity in the test section is monitored through a Mensor DPG 2400 dynamic pressure transducer, which is fed by a pitot tube upstream of the model in the test section. The free stream velocity is manually set through the wind tunnel engine RPM dependent on the monitored dynamic pressure. The experiments are conducted at free stream velocities of 5 and $10 [m/s]$.

3.5 Boundary layer model

Figure 3.6 shows the wind tunnel model which is used to create the laminar boundary layer over the tested ns-DBD plasma actuator. This model has a super-elliptical leading edge to damp down instabilities due to surface imperfections [Lin et al. (1992)]. This leading edge has a smooth transition to a flat surface with a groove over the full span of the model. In this groove the tested ns-DBD plasma actuator is flush mounted to the models surface. The opposite side of the model has been used for backward facing step experiments. The model is $400 [mm]$ wide, $450 [mm]$ long with the super-elliptical section extending to $110 [mm]$ from the leading edge. The groove for flush mounting is $20 [mm]$ wide and starts at $150 [mm]$ from the leading edge of the model. The flat surface of this model, in which the ns-DBD plasma actuator is flush mounted, is set parallel to the free stream velocity.

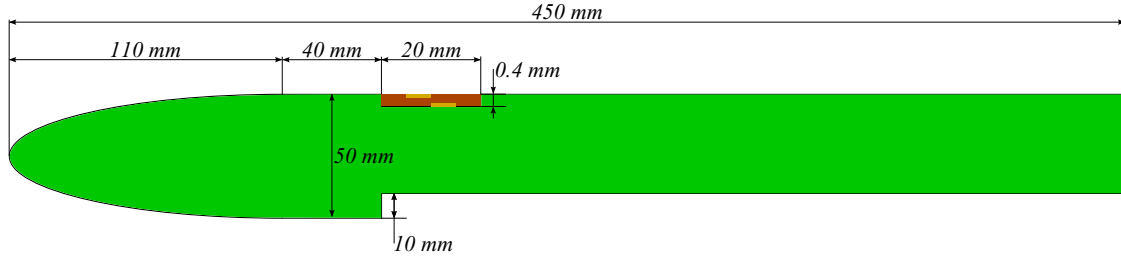


Figure 3.6: Schematic representation of the boundary layer model, with exaggerated ns-DBD plasma actuator and groove scaling for clarity.

3.6 Particle Image Velocimetry

Planar Particle Image Velocimetry (hereafter called PIV) is used to determine the laminar boundary layer velocity field over the flush mounted ns-DBD plasma actuator. The complete set-up is shown schematically in side-view in figure 3.7. The measurement plane is in the spanwise middle of the boundary layer model. A 20 [mm] high and approximately 1 [mm] thick laser sheet is shot in upstream direction perpendicular to the surface of the wind tunnel model. The sheet is formed with the use of a system of lenses and mirrors and a Quantel Big Sky Laser Twins BSL 220 (CFR 400-30-THG-WS). This is a double-pulsed Nd:YAG laser with a maximum energy of 220 [mJ] per pulse and a pulse duration of 7 [ns]. PIV tracer particles are introduced into the flow at the inlet of the wind tunnel by a Safex Fog Generator 2010 supplied with Safex Fog Fluid Normal Power Mix. These particles have a density of 1000 [kg/m³] and a size of between approximately 1 – 3 [μm]. PIV image pairs are recorded with a La Vision Imager pro LX 16M camera which has a 4870 pixels × 3246 pixels CCD sensor with a pixel pitch of 7.4 [μm] × 7.4 [μm]. A Nikon ED AF Micro Nikkor 200 [mm] 1:4 D lens with Soligor Extension Tubes was used to set the Field Of View (FOV) of this PIV system to 28.65 [mm] × 19.08 [mm] equaling a Magnification (M) of 1.26.

Image acquisition frequency is set at 0.5 [Hz]. Flow disturbances in the 5 [m/s] freestream will have traveled 10 [m] before a new image pair is acquired. This means the disturbance is very much out of the FOV and phase-locking can be applied. The time step (Δt) between the two laser pulses was set at 40 [μs] for 5 [m/s] free stream velocity experiments, while 20 [μs] is used for 10 [m/s] experiments. The setups internal delay from the laser trigger pulse to the plasma discharge was measured with a high voltage probe and an oscilloscope to be 11 [μs]. The Tektronics AFG3252 Arbitrary Function Generator used in these experiments has a minimal trigger delay of 100 [μs], which led to the decision to neglect this internal delay. Moreover, a result indicated as acquired 0 [ms] after the discharge burst, indicates that there is no delay between image-pair acquisition and the end of the discharge period. An example is a burst of 5 pulses at 10 [kHz] which has a trigger delay of 1.9995 [s] from the first laser pulse to the start of image-pair acquisition, in order to acquire 0 [ms] after discharge. This is schematically shown in figure 3.9.

Post-processing of the acquired image pairs to PIV vector fields is done with the Davis 8.2 software package. For every single image pair a multi-pass cross-correlation was used, were

an initial interrogation window size of $64 \text{ pixels} \times 64 \text{ pixels}$ with 50 % overlap was twice passed and a final window size of $16 \text{ pixels} \times 16 \text{ pixels}$ with 50 % overlap was also passed twice. This results in a velocity vector field with $21.2 [\text{vectors}/\text{mm}]$. All tested sets of image-pairs are processed using Sum-of-Correlation (*SOC*), which means the correlation maps of all phase locked separate image pairs are summed. The final correlation map, leading to a vector field, is the most correct solution because outliers due to optical aberrations in the high magnification image pairs have a lower contribution in the final result. Every tested set consists of 300 separated phase-locked image pairs.

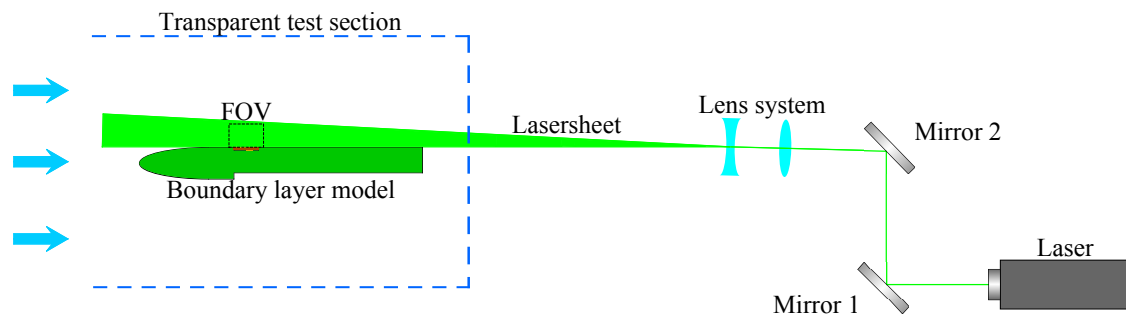


Figure 3.7: Schematic representation of the setup with the boundary layer model in the W-tunnel. Size of the ns-DBD plasma actuator and laser sheet optics exaggerated for clarity.

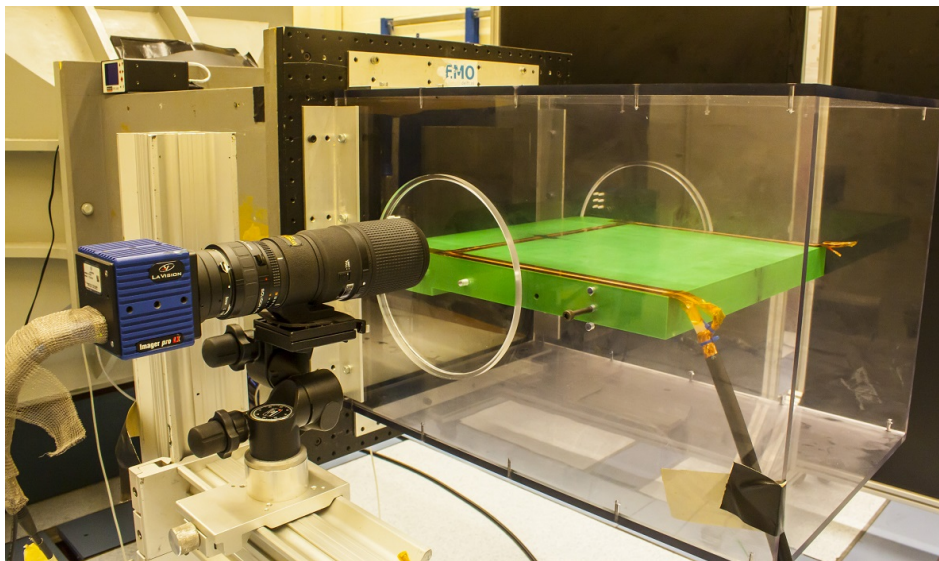


Figure 3.8: Photograph of the setup with the boundary layer model in the transparent test section of the W-tunnel.

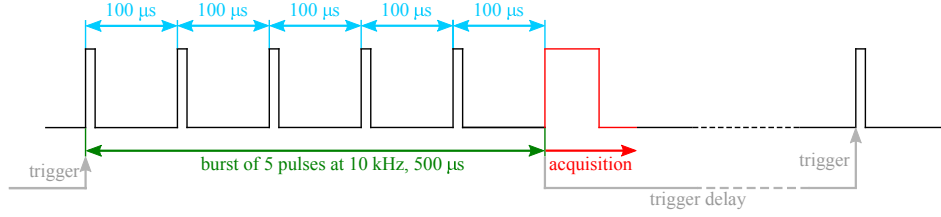


Figure 3.9: Scheme of acquisition timing in the PIV experiment. The example shows a discharge burst of 5 pulses with image acquisition 0 [ms] after the discharge burst has ended.

3.7 Energy measurements

The electrical performance of the barriers is compared based on the energy associated with the plasma discharge of tested actuators. The back-current shunt technique is used to measure the voltage of pulses traveling through the grounded outer shielding of the high voltage coaxial cable. The shunt is placed in the middle of the 20 [m] high voltage coaxial cable (type RG-217) which is used to connect the tested plasma actuator to the used power generator. This shunt consists out of 16 resistors of 3.2 [Ω] placed in parallel (equaling $R_{shunt} = 0.2$ [Ω]) in the outer shielding of the cable. A normal BNC cable connects both ends of the shunt to a Tektronics TDS3054C 1GHz digital oscilloscope, such to measure the voltage over the shunt. To protect the oscilloscope from voltage overload during testing, an attenuator of -20 [dB] is placed between the shunt BNC cable and the oscilloscope.

This shunt gives a theoretical attenuation factor (K_{sh}) of 250 [–]. This is related to the high voltage cable impedance ($Z_{cable} = 50$ [Ω]), the resistance of the shunt (R_{shunt}) and the voltages to the actuator and over the shunt ($U_{actuator}$ and U_{shunt}). This relation is shown in equation 3.1. Calibration was performed by applying a known 5 [V] signal over the high voltage cable and measuring the voltage over the shunt. The calibration voltage was supplied by the Tektronis AFG3252 arbitrary function generator and both the voltage over the shunt and input voltage were measured directly with the Tektronics TDS3054C 1GHz digital oscilloscope. This oscilloscope was set to the same impedance of the high voltage cable. The calibration process yielded a $K_{sh} = 303.02$ [–] for the shunt (without the separate attenuator).

A measurement of the voltage over the shunt during the discharge of a single pulse by the tested ns-DBD plasma actuator will give a readout on the oscilloscope of the attenuated voltage (of both shunt and separate attenuator). The first voltage peak measured is the voltage pulse traveling to the tested ns-DBD plasma actuator. The second peak is the voltage pulse reflected back through the cable after a single pulse discharge. The total energy contained in each measured pulse may be calculated with equation 3.2, where V is the voltage in the cable and Z is the impedance of the cable [Dworsky (1980)]. The total energy per discharge pulse can be determined for the input pulse (E_{in}) and the reflected pulse (E_{out}). The difference between the energy of the input pulse and the reflected pulse ($E_{pp} = E_{in} - E_{out}$) is the energy

deposited to the flow and dissipated in the ns-DBD plasma actuator.

$$K_{sh} = \frac{Z_{cable}}{R_{shunt}} = \frac{U_{actuator}}{U_{shunt}} \quad (3.1)$$

$$E_{in} = \int P_{in} dt = \int V_{in} I_{in} dt = \int \frac{V_{in}^2}{Z} dt \quad (3.2)$$

3.8 Barrier material tests

A comparison between the different barrier materials can only be made when all relevant material specifications are known. The supplied manufacturer data was not sufficient for a complete comparison, which is why new measurements are needed. The dielectric constant (η_r), electrical volume resistivity (ρ_{vr}) and thermal conductivity (k) are tested for the barriers used in the Schlieren experiments.

The dielectric constant (η_r), or relative permittivity, of the barrier materials is determined by measuring the capacitance (C) of a dedicated test sample. This test sample is a circular parallel plate capacitor, which consists of a disc of 20 [mm] of the tested barrier material with an electrode on either side of it. These electrodes are made of gold and are sputtered on the surface of the sample using a Balzers SCD 040 sputtering device. They are 10 [nm] thick and have a diameter of 20 [mm] on one side of the disc and 14 [mm] on the opposite side so to avoid short-circuit problems and alignment errors. The capacitance (C) was measured with an accuracy of $0.01 \cdot 10^{-12}$ [F] by connecting the sputtered electrodes to an Agilent 4263B LCR Meter, which is set at a frequency of 1 [kHz] and a voltage of 1 [V]. This is shown in figure 3.10(a) The dielectric constant (η_r) can be calculated through equation 3.3, with the absolute dielectric permittivity of vacuum ($\eta_0 = 8.854 \cdot 10^{-12}$ [F/m]), the barrier thickness (t_b) and the electrode overlap area (A).

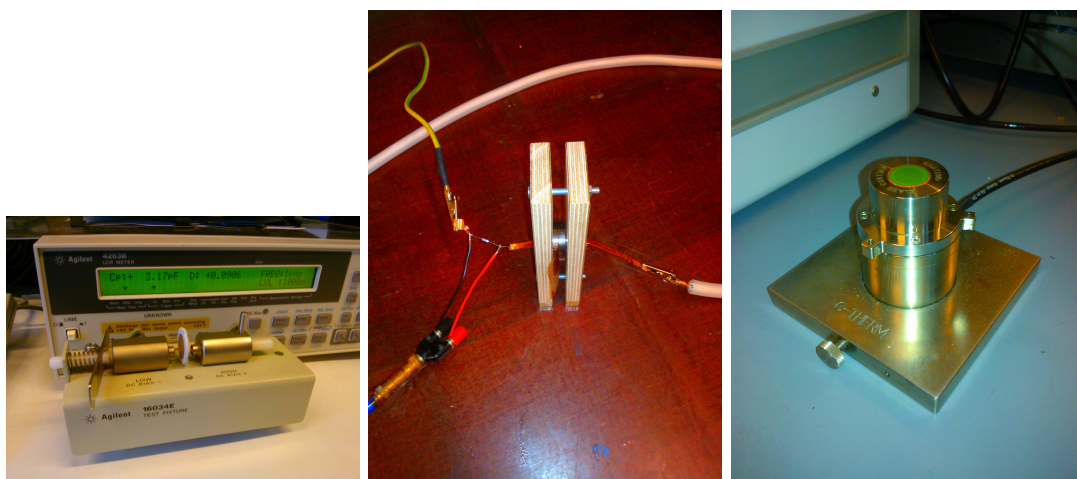
$$C = \eta_0 \eta_r \frac{A}{t_b} \quad (3.3)$$

The electrical volume resistivity (ρ_{vr}) is determined by measuring the resistance (R_b) of a test sample of barrier material. This sample of a measured thickness (t_b) is fixed between two aligned electrodes which have a diameter of 35 [mm]. The setup is shown in figure 3.10(b). The resistance of the sample is determined by applying a known DC voltage of 15 [kV] to the electrodes and measuring the current through the barrier. The application of the voltage and measurement of the current is performed with a TREK model 20/20c-hs high voltage amplifier connected to a computer with LabView software. Moreover, the assumption is made that the resistance of this small electrical system is much lower than the barrier resistance (R_b) and can therefore be neglected. Measurements of voltage and current are taken over a

duration of 60 [s] at a frequency of 1 [kHz], which each sample consisting of a 100 samples at 100 [kHz]. Finally, the volume resistivity (ρ_{vr}) is calculated through equation 3.4.

$$\rho_{vr} = R_b \frac{A}{t_b} \quad (3.4)$$

The thermal conductivity (k) of the barrier materials was measured on new test samples, without electrodes, through a C-Therm Technologies TCI^{TM} thermal conductivity system. This system uses a modified transient plane source technique as described by Log and Gustafsson (1995). This system applies a small temperature rise to the material after which a cooling down period is used to measure the thermal conductivity of the material. This is why measurements of the tested barrier materials are taken of the thickest barrier available for each single layer material. The setup is shown in figure 3.10(c). The machine was calibrated with a piece of acrylic glass.



(a) Capacitance measuring.

(b) Resistance measuring.

(c) Thermal conductivity measuring.

Figure 3.10: Measurement setups for the tested barriers material properties.

Chapter 4

Barrier material dependent energy deposition

The effect of different barrier materials on the discharge and energy deposition of an ns-DBD plasma actuator is quantified and discussed in this chapter. An ns-DBD plasma actuator of constant electrode dimensions is constructed with three different barrier materials and three different barrier thicknesses, as described in section 3.1. The chosen barrier materials are Kapton[®] Polyimide tape (hereafter called Kapton), Silicone-rubber (hereafter called silicone) and Fine Polyamide PA2200 (hereafter called PA2200). The material specifications of these barriers which are relevant for this investigation are measured. The effect of these barriers on the effectiveness of energy deposition of the ns-DBD plasma discharge is investigated with Schlieren imagery (section 4.2). Moreover, discharge characterization (section 4.3), calculations of volumetric heating (section 4.4) and energy measurements (section 4.5) are conducted. This chapter is concluded with a short discussion of the results.

Background, setup, results and conclusions of this investigation have already been published in a conference paper, by Winkel et al. (2014). A journal paper by Correale et al. (2015) containing this work is under review.

4.1 Barrier material specifications

Three characteristics of the barrier materials were determined, namely the dielectric constant (η_r), the electrical volume resistivity (ρ_{vr}) and the thermal conductivity (k). The results presented in this section originate from the tests described in section 3.8. An overview of the final results is shown in table 4.1.

The dielectric constant (η_r) was tested only once for every test sample and not every variation of barrier material with barrier thickness was tested. This was because of a combination of time and material constraints. The dielectric constant (η_r) is calculated with the use of equation 3.3 and the result is shown in figure 4.1(a). The assumption is made that a

linear relation between capacitance (C) and barrier thickness (t_{bl}) exists, which implies that the dielectric constant is independent on barrier thickness. Therefore, the average of all the determined dielectric constants per material is taken as the mean dielectric constant of that material. The final values are shown in table 4.1. The dielectric constant (η_r) of the tested silicone is on average slightly higher than that of the tested Kapton, while PA2200 is significantly more dielectric. However, large differences exist in dielectric constant between test samples of silicone. Individual samples are tested multiple times to check repeatability of the measurement. Unfortunately, local differences in the material properties of a large material sample and correctness of the sputtered electrodes cannot be averaged over the results. This is because only one sample is tested for a specific combination of barrier material and thickness.

Determined values of electrical volume resistivity (ρ_r) for the tested materials are shown in figure 4.1(b). The results indicate a strong dependency on the barrier thickness, which is possibly caused by impurities in the material. Applying more layers of Kapton tape to each other will enclose more impurities of air and dust between the layers. Moreover, thicker sheets of silicone and PA2200 will have manufacturing impurities of their own. Measured resistance (R) was also dependent on the applied DC voltage, with a higher voltage giving less noise in the measured current and resulting in higher resistance values. However, the highest determined values of electrical volume resistivity (ρ_{vr}) are more than a factor 1000 lower than little manufacturing data available. Therefore, the thinnest barrier is chosen as an indication for the electrical volume resistivity (ρ_{vr}) of that material. These values are shown in table 4.1. As expected the resistivity (ρ_{vr}) of the tested Kapton is much higher than the tested silicone. PA2200 has a similar resistivity (ρ_{vr}) to silicone while having a different material structure.

Results of the thermal conductivity (k) tests are shown in table 4.1. Measurement are taken after selecting a certain material group in the calibration process of the program and selecting a dry or wet (distilled water) contact surface. If the measurement does not converge after a few repetitive measurements this indicates that a wrong setting was selected. All values shown in table 4.1 are of converged tests. This shows that the tested Kapton and silicone barriers have a similar thermal conductivity (k). The tested PA2200 barrier has a much lower thermal conductivity (k), which can be accredited to the more porous structure.

Table 4.1: Properties of the tested barrier materials.

Symbol	Description	Barrier material:		
		Kapton	silicone	PA2200
η_r	Dielectric constant [-]	2.9	3.0	3.6
ρ_{vr}	Electrical volume resistivity [Ωm]	$2.97 \cdot 10^9$	$3.41 \cdot 10^8$	$4.0 \cdot 10^8$
k	Thermal conductivity [$\frac{W}{mK}$]	0.29	0.27	0.1

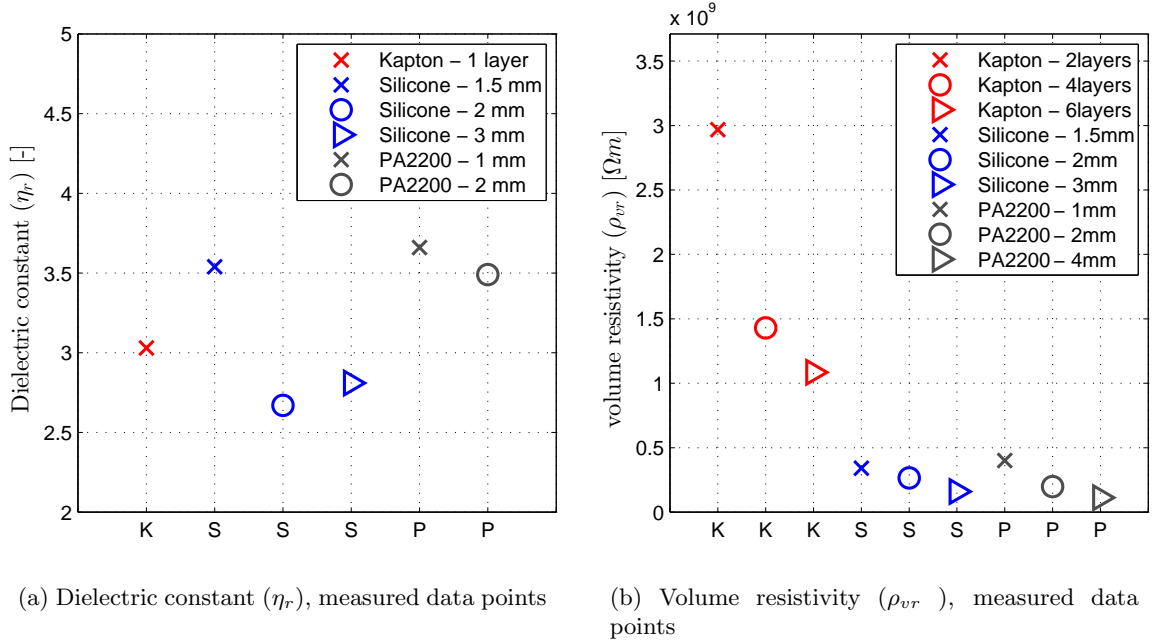


Figure 4.1: Measured barrier material properties.

4.2 Schlieren results

The introduced disturbance by discharge of the tested ns-DBD plasma actuator is acquired with the use of Schlieren images. In this section the structure of this disturbance is discussed. Figure 4.2 shows the evolution of the disturbance growth and propagation in the quiescent air above a ns-DBD plasma actuator with a 2 layer Kapton barrier, 1.5 [mm] thick silicone and 1 [mm] thick PA2200 barrier. Images are shown depending on the number of pulses applied, hence the energy input to the actuator. Thus 20 pulses implies that the image shows the accumulative effect of all preceding discharge pulses and the shock wave of the 20th pulse. These images show that:

- The induced density gradient by an ns-DBD plasma actuator with a 2 layer Kapton barrier at 20 and 100 pulses has a similar structure. A fixed area of density change is connected to the wall between approximately $x = 0$ and -5 [mm] at the location of the plasma discharge. An additional mushroom shaped area is rising and growing from between $x = 0$ and -2 [mm]. At 1000 pulses the mushroom shaped disturbance shows less structured buoyancy effects and is skewed to the negative x-direction. However, the disturbance propagation does not appear to be affected by the weak shock wave. Moreover, only a single weak shockwave is visible, which is in agreement with the results for a pulse width shorter than 200 [ns] of [Benard et al. \(2012\)](#) (shown in figure 2.4).
- The density gradient for the case of an ns-DBD plasma actuator with a 1.5 [mm] silicone barrier has a very different structure compared to one with a Kapton barrier. The area

between $x = 0$ and approximately $-5 [mm]$ where plasma discharge is located on the surface of the barrier is also the area where the main density change is visible. Small circular structures are visible at $x = -10 [mm]$ and $x = 5 [mm]$. In a time resolved sequence these structures rotate like vortices in clockwise direction at $x = -10 [mm]$ and counter-clockwise direction at $x = 5 [mm]$. This indicates that during the discharge a small amount of air is accelerated. Additionally, it shows that a small secondary plasma discharge area is created. At 1000 pulses the accumulated effect of the small acceleration in negative x-direction is more strongly visible. The density field disturbance is stretched out over a larger area in negative x-direction, while less vertical movement is visible than in the case of an actuator with a Kapton barrier. The weak shock wave is much less pronounced in these results compared to the results for the ns-DBD plasma actuator with a Kapton barrier. This is accredited to the longer exposure time of $5 [\mu s]$ used for the image acquisition, relative to the $2 [\mu s]$ for the other materials.

- The density gradient results for the ns-DBD plasma actuator with a $1 [mm]$ PA2200 barrier are similar to one with a silicone barrier, with the addition of a wall normal component emanating from $x = -1 [mm]$. However, the two rotating structures are less clearly visible. The secondary discharge at the $x = 5 [mm]$ is less pronounced visible, but still present. The acceleration of the flow in negative x-direction is present similar to the results of the ns-DBD plasma actuator with a silicone barrier. A slight misalignment of the Schlieren setup is visible with light of density gradient change visible below the $y = 0 [mm]$ axis. This means some details of the induced density field structure could be lost. However, the weak shock wave is clearly visible for this case. Another observation is that the shock wave position fluctuates in position between the application of 20, 100 and 1000 pulses. This is caused by the power generator, which in the case of an ns-DBD plasma actuator with PA2200 barrier has difficulty to provide consistent pulse frequency for the discharge. This is probably due to the larger energy consumption by this and the silicone barrier (as will be shown later), indicating the need for longer recharge times of the power generator.

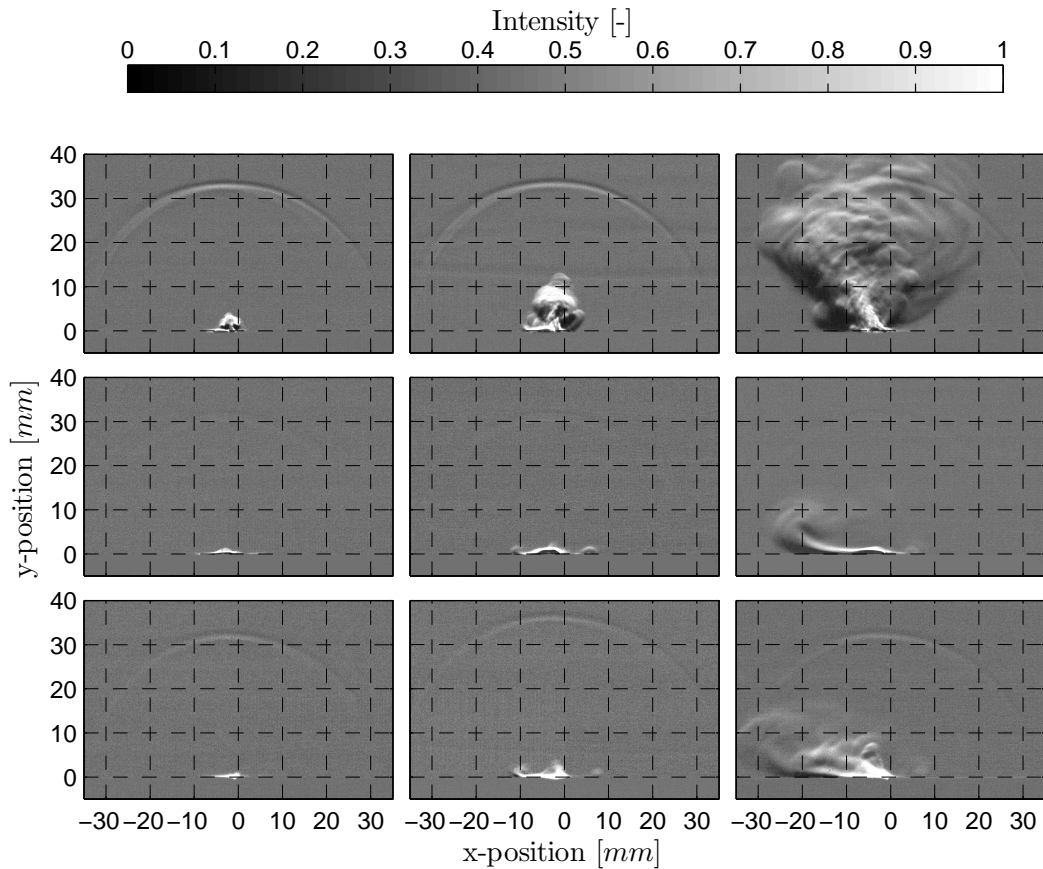


Figure 4.2: Evolution of the disturbance in quiescent conditions shown by Schlieren density gradients normal to the wall. Difference to undisturbed density gradient field is visualized 0 [ms] after a discharge burst at 10 [kHz] for the three tested materials.

4.3 Discharge characterization

The ns-DBD plasma actuator discharge structure is photographed as described in section 3.3. The thickness of the tested materials is equalized as much as possible for this comparison. Therefore an ns-DBD plasma actuator with a Kapton barrier of 11 layers (0.979 [mm]) is compared to actuators with a 1.5 [mm] thick silicone barrier and 1 [mm] thick PA2200 barrier. The ns-DBD plasma actuators are fed with a 0.1 and 1 [kHz] and signal at 10 [kV] applied voltage for these tests.

The 50 [mm] of discharge in the middle of the discharge areas of the three tested barriers is shown in figure 4.3. These discharges are created with a 10 [kV] signal at 1 [kHz]. The discharge structure or morphology is of filamentary nature in all cases.

- The ns-DBD plasma actuator with a Kapton barrier has the complete visible discharge area located above the covered high voltage electrode, thus between approximately $x = -5 [mm]$ and $x = 0 [mm]$. The discharge has a few filaments visible within the otherwise smooth glow discharge.
- The ns-DBD plasma actuator with a silicone barrier shows visible light emitted from the area above the covered high voltage electrode between $x = -5 [mm]$ and $x = 0 [mm]$. Additionally, visible light is captured by the camera at the opposite side of the exposed electrode, at $x = 5 [mm]$. In the main discharge the plasma is more filamentary at the edge of the exposed electrode relative to the Kapton case. The bright filaments are shorter than in the Kapton case and resulting in a diffuse glowing structure. In the secondary plasma discharge no streamers are visible, implying a smooth glow discharge is present.
- The ns-DBD plasma actuator with a PA2200 barrier has a much more pronounced filamentary discharge behavior above the covered electrode than both the Kapton and silicone cases. This is due to the more porous nature of the PA2200 barrier material relative to the other materials. A secondary light emittance by plasma discharge at $x = 5 [mm]$ is visible, which is both shorter and brighter than the one in the silicone case.

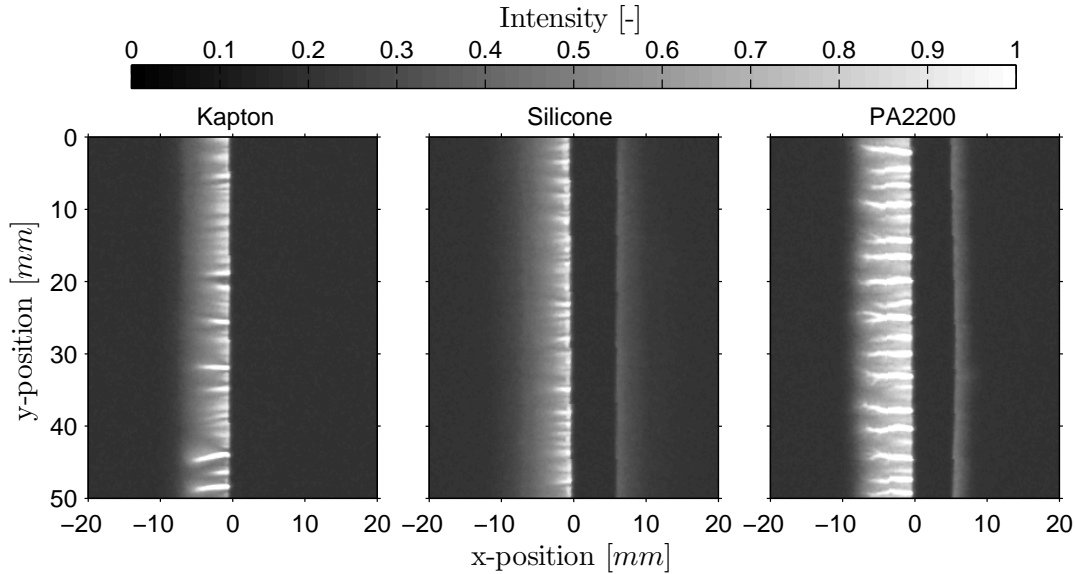


Figure 4.3: Characterization of the discharge structure of the three materials, tested at $1 [kHz]$ with an exposure time of $1 [s]$.

The average light intensity over the same $50 [mm]$ length of the middle of the discharge domain is shown in figure 4.4. Discharge at both 0.1 and $1 [kHz]$ is shown. These graphs show that the light intensity is proportional to the discharge burst frequency for all tested ns-DBD plasma actuators. The graphs confirm that light is emitted from both sides of the exposed electrode in the case of an ns-DBD plasma actuator with a silicone or PA2200 barrier. This is visible with an extra light intensity peak starting at $x = 5 [m/s]$. Both these materials have a

lower electrical volume resistivity (ρ_{vr}) compared to the tested Kapton barriers (as shown in table 4.1). The lower resistivity implies electrons are able to diffuse easier through the barrier towards areas with a lower electrical potential. This results in a discharge on both sides of the grounded exposed electrode. The ns-DBD plasma actuators with a Kapton or silicone barrier have a similar average light intensity in the area above the exposed electrode. However, the silicone case has a more smooth decrease to zero light emittance at around $x = -10$ [mm]. PA2200 has in both cases the brightest discharge over the full width of the covered high voltage electrode, but has a shorter discharge length on both sides of the exposed electrode than the silicone case.

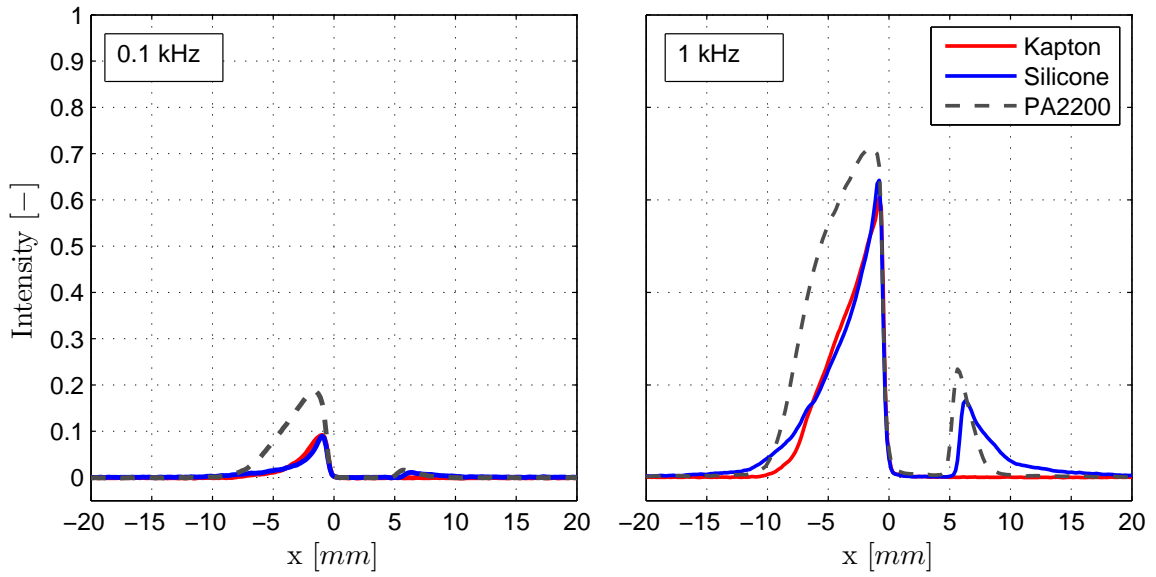


Figure 4.4: Average discharge light intensity of the three materials, measured over the middle 50 [mm] of the discharge. Results at 0.1 and 1 [kHz] with an exposure time of 1 [s].

4.4 Volumetric heating by ns-DBD plasma discharge

The two dimensional area in the density gradient field which is disturbed by the tested ns-DBD plasma actuator can be determined from the Schlieren images. A Matlab[®] program is written to calculate the affected area. The program first subtracts an image without density field disturbance from the interrogated image in order to isolate the introduced disturbance. The disturbance is then isolated by setting thresholds on the mean image intensity. The values for these thresholds (based on mean intensity and a factor of the standard deviation) are set by trial and error for each individual image. Unavoidable gaps in the result are smoothed out with a two dimensional smoothing function. The radius (R_{smooth}) in this function is another value that is set through trial and error. The final area of disturbance is calculated by counting the pixels which are set to contain 'disturbed area' and multiplying this with the

dimensional calibration. This allows the evolution of the disturbed area to be tracked in time. An example of an interrogated image and the resulting determined area of density field disturbance is shown in figure 4.5.

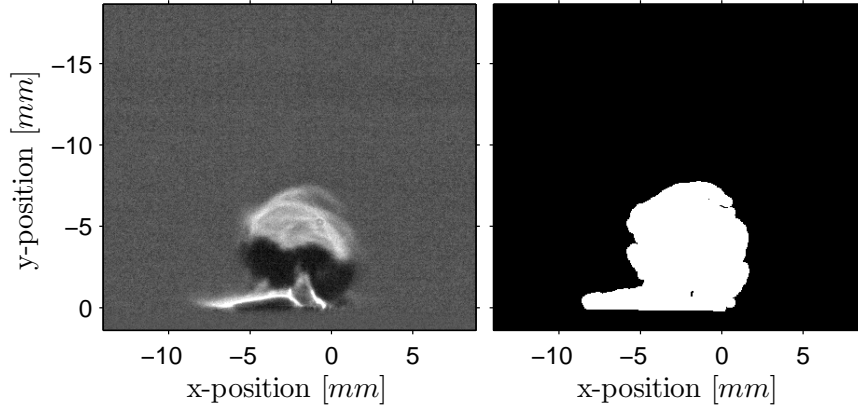


Figure 4.5: Demonstration of the area measurement technique used for the Schlieren experiments. Interrogated image on the left, determined disturbed area in white on the right.

The area of density field disturbance by the ns-DBD plasma actuator as a function of elapsed time from the beginning of the discharge is discussed for every barrier thickness and for every barrier material. These trends are visualized in figure 4.6 for the first 10 [ms] and up to 100 pulses of the tests. Calculated areas are available of up to 1000 pulses but buoyancy and thermal expansion introduce uncertainty in the area determination method when more than 100 pulse are applied.

The results in figure 4.6 show large differences in disturbed density field area in the quiescent air between the ns-DBD plasma actuators with the different barriers materials. The disturbed area by the ns-DBD plasma actuator with a Kapton barrier is about one order of magnitude higher than for actuators with a silicone or PA2200 barrier. Additionally, an almost linear growth is observed for the three tested Kapton cases while the discharge is on. This corresponds to previous results by [Michelis et al. \(2013\)](#) and [Correale et al. \(2014\)](#). Disturbance area over time is more irregular for the ns-DBD plasma actuators with silicone and PA2200 barriers. The thermal energy deposition per pulse is apparently lower for actuators with these barrier than with a Kapton barrier. Magnitudes of disturbed areas for a barrier made out of silicone are slightly higher than those of PA2200. Moreover, both of these barriers show a rapid decrease of the disturbed area when discharge has ended. The results show that independent of the barrier material an ns-DBD plasma actuator with a thicker barrier disturbs a smaller area of the density field. This implies that an actuator with a thicker barrier deposits less thermal energy to the near wall volume of air. This is a possible result of the larger distance between the two electrodes caused by a thicker barrier. This lowers the reduced electric field strength (E/N) between the electrodes, thereby weakening the discharge itself and the resulting thermal energy deposition.

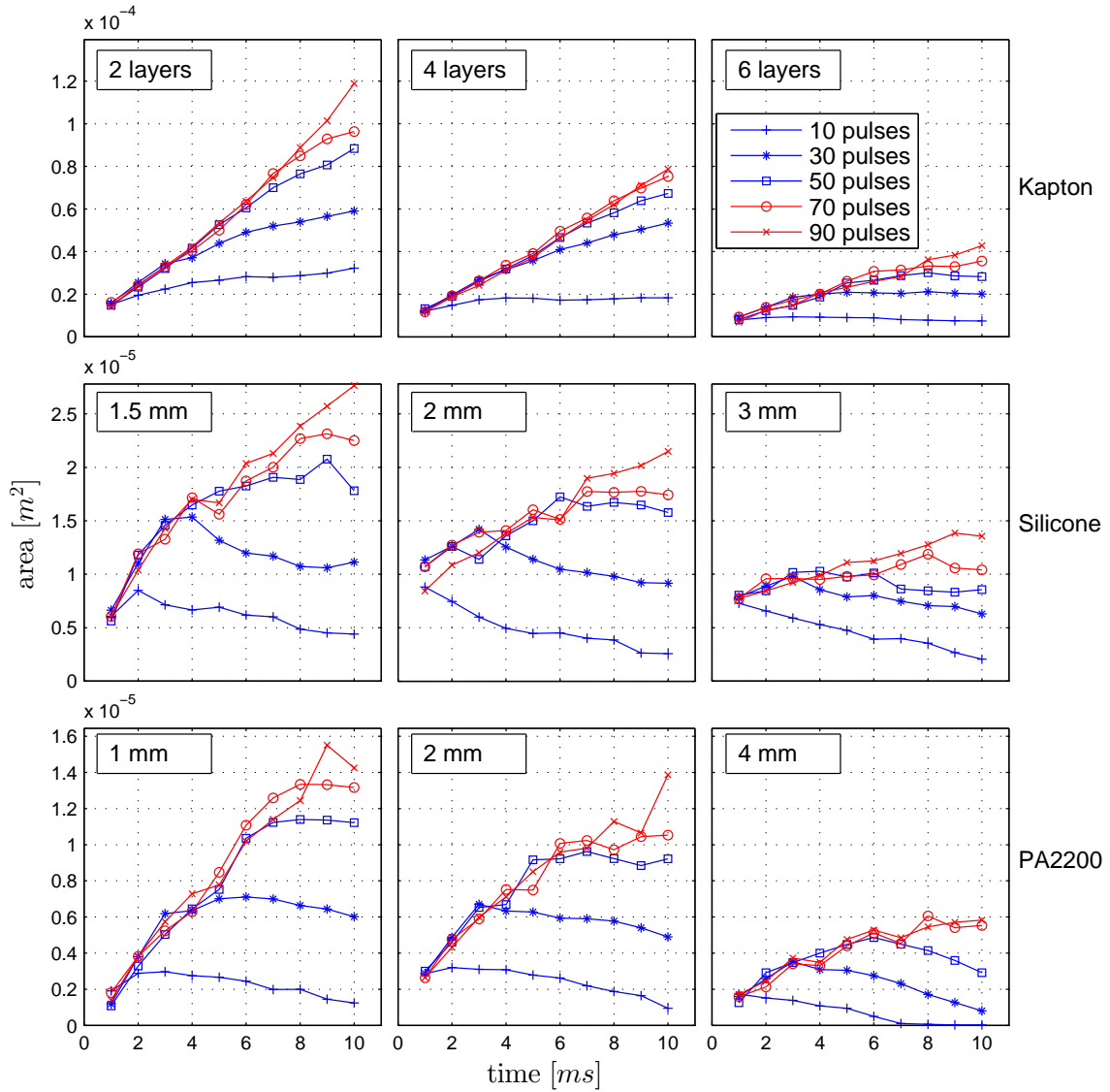


Figure 4.6: Growth of the disturbed density field area (A) over time with different amount of pulses. Results for the three tested barrier materials at their three tested barrier thicknesses. Discharge pulses at 10 [kV] and a frequency of 10 [kHz].

The disturbed area by discharge of ns-DBD plasma actuator dependent on the barrier thickness is shown in figure 4.7. This figure shows more explicitly that the disturbed area is always lower in case of less energy input (less applied pulses). An increase in barrier thickness always reduces the disturbed area when a Kapton barrier is used. For actuators with a silicone or PA2200 barrier a more irregular relation between discharge pulses and barrier thickness is noticeable. This can be caused by the different discharge regimes and discharge locations shown in section 4.3. Additionally, the smaller area of density field disturbance might affect the relative uncertainties in the area determination.

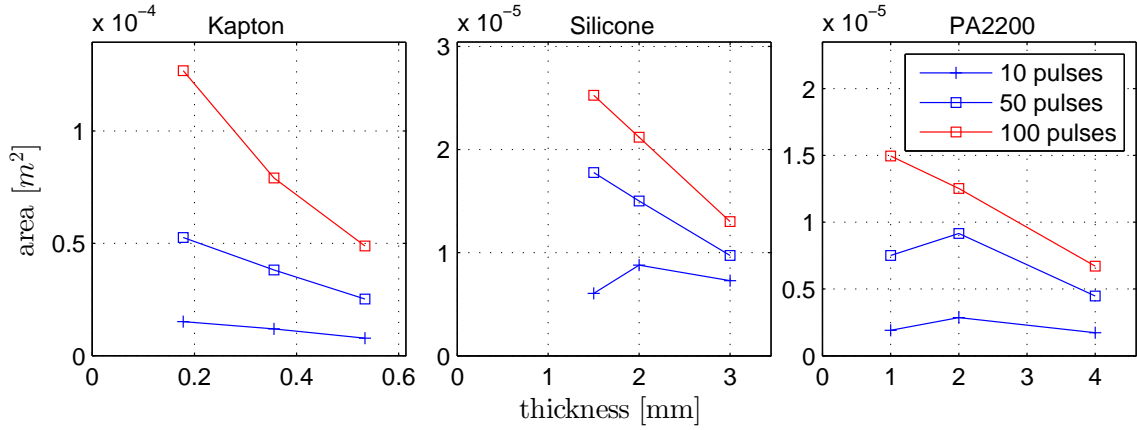


Figure 4.7: The area of the disturbed density field area over the three thicknesses for the three different barrier materials tested. Area measured directly after the application of the last discharge pulse. Discharge pulses at 10 [kV] and a frequency of 10 [kHz].

In figure 4.8 the time evolution is shown of disturbed area by thermal energy deposition scaled with barrier thickness for a constant energy input by a discharge burst of 30 pulses. The graphs for the three different barrier materials show that the relative area of disturbance is larger when a thinner barrier material is used. A linear increase of the relative area is apparent when discharge is on, as earlier concluded from figure 4.6. This implies that each discharge pulse deposits the same amount of thermal energy to the near wall volume of air, with the amount dependent on barrier thickness and material. Moreover, the steeper linear gradient when discharge is on implies that the thermal energy deposition per pulse is larger when a thinner barrier is used.

Results of relative disturbed area for the discharge with a Kapton barrier indicate that thermal expansion takes over after the discharge has ended, resulting in a non-linear behavior in time. This is in small amount also visible for the case of a 1 [mm] PA2200 barrier. However, the relative heated area after discharge by a ns-DBD plasma actuator with a silicone barrier reduces. The thermal conductivity (k) of the Kapton and Silicone barriers is very similar, as was shown in table 4.1. This means that the rate of thermal energy conduction through the barrier should be similar. However, the silicone barrier is thicker than the Kapton barrier, resulting in a larger volume of material in which thermal energy can be deposited. The difference in thermal expansion is therefore attributed to the possible different thermal capacity, or heat capacity, of the materials. A larger thermal capacity is able to suppress the thermal expansion by absorbing more heat. The difference between thermal expansion after discharge of the cases with a silicone and PA2200 barrier material can be accredited to the comparatively lower thermal conductivity (k) of the PA2200 material.

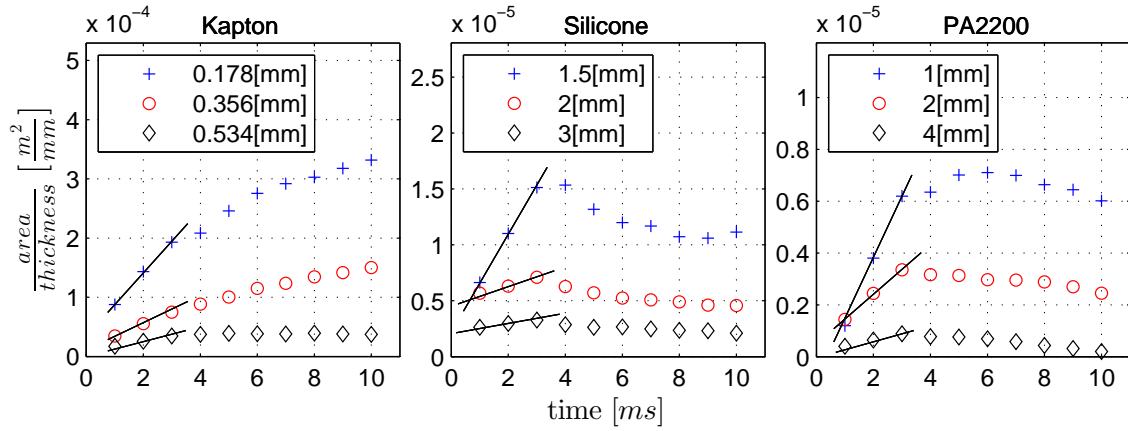


Figure 4.8: The ratio of disturbed area to the thickness of the barrier for the first 10 $[\mu s]$ of the experiment for the three different barrier materials tested. Data of a discharge burst of 30 pulses is shown. Discharge pulses at 10 [kV] and a frequency of 10 [kHz].

4.5 Energy measurements

Due to the different electrical and thermal properties of the barrier materials in the ns-DBD plasma actuator the conversion from electrical to thermal energy will be different as well. Therefore electrical energy measurements are made to compare the different materials.

In figure 4.9 the input and reflected voltage pulses are shown for for a single pulse discharge of the tested ns-DBD plasma actuator with the three different barrier materials. These values are measured with the use of the back-current shunt technique discussed in section 3.7. The energy input (E_{in}), reflected back (E_{out}) and used for the discharge per pulse (E_{pp}) is calculated through equation 3.2 and shown in table 4.2. While the energy input is similar in all three materials, the reflected energy is different for different materials tested. The the relative energy deposited to the surrounding air and dissipated in the barrier compared to the energy input (E_{pp}/E_{in}) is about 4.5 times higher for the Silicone and PA2200 barriers than for the Kapton barrier.

The disturbed density field area is not available for a ns-DBD plasma actuator with a barrier made out of 11 layers of Kapton, which makes comparison to the PA2200 barriers difficult. A power law interpolation is fitted to the experimental data such to approximate the disturbed area by an ns-DBD plasma actuator with a 11 layer Kapton barrier. The power law is of the form shown in equation 4.1. The constants of values $a = 0.62$ and $b = 2.11 \cdot 10^{-4}$ where found to give the smallest error to the experimental data for the discharge bursts of 100 pulses. In figure 4.10 the interpolation and experimental data points are shown. This interpolation yields an approximate disturbed density area of $1.48 \cdot 10^{-5} [m^2]$. Finally, this approximations and the corresponding experimental values for the actuators with silicone and PA2200 barrier

materials are shown in table 4.2.

$$A(\text{layers}) = b \cdot (a)^{\frac{\text{layers}}{2}} \quad (4.1)$$

It can now be determined that an ns-DBD plasma actuator with a barrier made out of silicone uses approximately 4.4 times more energy per pulse (E_{pp}) to produce an approximately 1.7 times larger disturbed area (A) than an actuator with a barrier made out of Kapton. Moreover, an actuator with a PA220 barrier uses approximately 4 times more energy per pulse (E_{pp}) to produce a similar disturbed area (A) than Kapton. Data from table 4.1 indicates that both PA2200 and silicone and have a 7.5 – 10 times lower electrical volume resistivity (ρ_{vr}) than Kapton which allows more electrical energy transfer through the barrier. This characteristic could explain the less efficient transfer from electrical energy to thermal energy by the ns-DBD plasma actuators with silicone and PA2200 barrier materials.

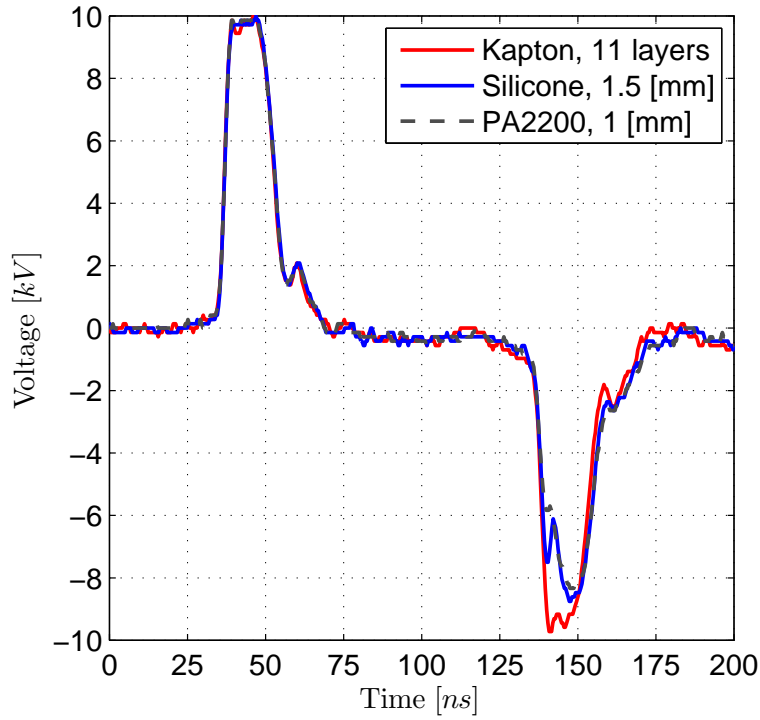
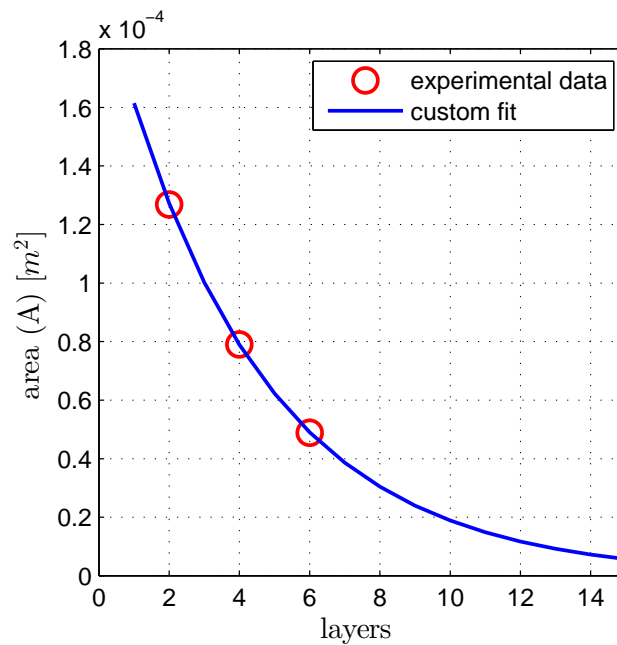


Figure 4.9: Voltage as a function of time for the three tested barrier materials. Discharge pulse initiated by a 10 [kV] voltage pulse.

Table 4.2: Energy associated with the discharge of the tested ns-DBD plasma actuators.

Energy	Barrier specification		
	Kapton	Silicone	PA2200
	11 <i>layers</i>	1 <i>layer</i>	1 <i>layer</i>
	0.979 [mm]	1.5 [mm]	1 [mm]
E_{in} [mJ]	28.00	29.02	27.74
E_{out} [mJ]	25.86	19.66	19.18
E_{pp} [mJ]	2.14	9.36	8.56
E_{pp}/E_{in} [-]	0.07	0.32	0.31
Disturbed area (A) for a burst of 100 pulses [m^2]	$1.48 \cdot 10^{-5}$	$2.53 \cdot 10^{-5}$	$1.5 \cdot 10^{-5}$

**Figure 4.10:** Interpolation of the disturbed density area for the results of an ns-DBD plasma actuator with Kapton barrier fed with a burst of 100 pulses at 10 [kV] and 10 [kHz].

4.6 Discussion

In this chapter the influence of the barrier used in the tested ns-DBD plasma actuators was investigated. Thermal energy deposition was determined with the use of Schlieren imagery, while discharge intensity and morphology was measured through direct imaging. Additional, electrical energy usage by the ns-DBD plasma actuators was measured with the back-current shunt technique.

- Schlieren images of the density field disturbance in quiescent conditions by the discharge of the tested plasma actuators show a weak shock wave and a density change originating from the discharge area. The structure of this density field disturbance shows strong dependency on the barrier material. More thermal energy is created by the plasma reactions at higher values of reduced electric field strength (E/N). Moreover, the plasma discharge has a different structure and location, depending on the barrier material. Therefore, it is possible that an actuator with a PA2200 barrier with a bright filamentary discharge, has different plasma reactions at different locations than an actuator with a Kapton barrier. Thereby creating differences in structure of disturbance in the density field.
- Both the ns-DBD plasma actuators with a silicone and a PA2200 barrier have discharge on both sides of the exposed electrode. The secondary discharge at the opposite side of the exposed electrode relative to the covered HV electrode is accredited to the much lower electrical volume resistivity (ρ_{vr}) relative to Kapton. The porous structure of the PA2200 barriers is at the cause of the much brighter and filamentary plasma morphology of actuators with this barrier material.
- Independent of the barrier material, the disturbed density field area is in general larger for a thinner barrier. The steeper linear gradient when discharge is on for a thinner barrier relative to a thicker barrier implies that the thermal energy deposition per pulse is larger when a thinner barrier is used. This is attributed to the smaller distance between the two electrodes when the tested ns-DBD plasma actuator is fitted with a thinner barrier. This increases the reduced electric field strength (E/N), this increases the dissociation of air particles which results in thermal energy deposition.
- Growth of the disturbed density area is linear while discharge is on for an ns-DBD plasma actuator with a barrier made out of Kapton. This is similar to the experimental results by [Michelis et al. \(2013\)](#) and [Correale et al. \(2014\)](#). The same applies for the actuator with silicone and PA2200 barriers. In general more energy input (by discharge pulses) results in a larger disturbed density field area. An ns-DBD plasma actuator with a Kapton barrier has a disturbed density field area of approximately one magnitude larger than the an actuator with a silicone or PA2200 barrier. Of the latter two ns-DBD plasma actuators with a silicone barrier produce a larger area of disturbance.
- Thermal expansion after discharge has ended is strongly dependent on the barrier material. The similar thermal capacitance (k) of Kapton and silicone implies that the disturbed area reduction in silicone can be a function of the heat capacity of the barrier. The volume of the silicone and PA2200 barriers is larger, which results in a larger volume to which heat can be dissipated. Differences in thermal expansion between of disturbed density field area with the use of a silicone and PA2200 barriers, are due

to a much lower thermal capacitance (k) for PA2200.

- Electrical energy measurements by back-current shunt technique indicated that an ns-DBD plasma actuator with a Kapton barrier uses less energy to produce relatively more disturbed density field area than an actuator with a silicone or PA2200 barrier. This implies that more electrical and thermal energy is absorbed and dissipated in silicone and PA2200 barriers, than in Kapton barriers. This can be accredited to the higher volume resistivity of the Kapton material, through which less electricity is conducted during discharge.

Chapter 5

Laminar boundary layer flow disturbance

The local influence of the thermal energy deposition by an ns-DBD plasma actuator in discharge on the velocity field of a laminar boundary layer is still a matter of discussion. For this reason the velocity field disturbance in a low velocity laminar boundary layer by ns-DBD plasma actuation is quantified through phase-locked planar Particle Image Velocimetry (PIV) and shown in section 5.2. Parameters in this study are the streamwise position of the covered high voltage electrode, the amount of electrical energy supplied to the system and the freestream velocity of the laminar boundary layer. Associated energy with the discharge is shown in section 5.3. The changes in the density field are approximated with a finite difference discretization of the compressible mass continuity equation. This discretization is shown in section 5.1, while the results are shown in section 5.4. This chapter is concluded with a short discussion of the results.

5.1 Discretization of the compressible mass continuity equation

Thermal energy deposition by ns-DBD plasma actuators implies that the density in the near wall volume will change. A quantification of this disturbed density field by ns-DBD plasma actuator in a laminar boundary layer is attempted with the use of the compressible mass continuity equation. This equation (shown in equation 5.1) is used for the calculation of the two dimensional density field. For computational use, a first order backward-time backward-space finite difference (BTBS-FD) approximation is made, which is shown in equation 5.2. This discretized equation relates the two dimensional velocity field (u and v -components) to both the initial undisturbed density field ($\rho_{i,j}^n$) and the perturbed density field ($\rho_{i,j}^{n+1}$). The time step (Δt) is the time between the (initial) undisturbed and the disturbed flow or density field, hence the duration of the discharge burst. This time step is divided in a hundred smaller steps, with the discretized equation evaluated a hundred times. This results in smaller absolute density steps per iteration, reducing the possibility of exponential growth

of the solution due to overshoots in the solution. Also the finite difference spatial step (s) is introduced also for additional numerical stability. This spacial step was set to 3 velocity field indices. The density values of the upstream boundary ($x \approx -10$ [mm]) and the boundary furthest away from the wall of the model ($y \approx 6$ [mm]) are equal to the initial undisturbed density field at sea level ($\rho_0 = 1.225$ [kg/m³]). By spatial marching from high to low y-position and low to high x-position in the Field of View (FOV) the boundary conditions and initial conditions (equation 5.3) are used to calculate the disturbed density field ($\rho_{i,j}^{n+1}$).

$$\frac{\partial \rho}{\partial t} + \left(\frac{\partial u}{\partial x} + \frac{\partial v}{\partial y} \right) \rho + u \frac{\partial \rho}{\partial x} + v \frac{\partial \rho}{\partial y} = 0 \quad (5.1)$$

$$\frac{\rho_{i,j}^{n+1} - \rho_{i,j}^n}{\Delta t} + \left(\frac{\partial u_{i,j}^{n+1}}{\partial x} + \frac{\partial v_{i,j}^{n+1}}{\partial y} \right) \rho_{i,j}^{n+1} + u_{i,j}^{n+1} \frac{\rho_{i,j}^{n+1} - \rho_{i-s,j}^{n+1}}{s\Delta x} + v_{i,j}^{n+1} \frac{\rho_{i,j}^{n+1} - \rho_{i,j-s}^{n+1}}{s\Delta y} = 0 \quad (5.2)$$

$$\begin{aligned} \text{Initial conditions (IC)} & \quad \left\{ \rho_{i,j}^n = \rho_0 = 1.225 \text{ [kg/m}^3\text{]} \right. \\ \text{Boundary conditions (BC)} & \quad \left\{ \begin{aligned} \rho_{0,j}^{n+1} &= \rho_0 \\ \rho_{i,0}^{n+1} &= \rho_0 \end{aligned} \right. \end{aligned} \quad (5.3)$$

5.2 Particle Image Velocimetry results

A Particle Image Velocimetry (PIV) experiment has been conducted on an ns-DBD plasma actuator with a barrier made out of 2 layers of Kapton tape. Velocity fields of the flow with and without disturbance from the discharge of the tested ns-DBD plasma actuator will be discussed. Tested parameters are the energy input per discharge burst, the free stream velocity and the streamwise position of the covered high voltage (HV) electrode. A clarification of this streamwise position is given in figure 5.1. Furthermore, not the complete FOV is resolved to vector fields. This was because in this study focus was on the effects within the boundary layer and not on the outer freestream.

5.2.1 Undisturbed velocity field

Figure 5.2 shows the non-dimensional boundary layer profile of the undisturbed boundary layer flow. These are compared to the theoretical Blasius boundary layer for both the 5 and 10 [m/s] free stream velocity. Corresponding shape factor (H) values are shown in table 5.1. Interpolation is used to set the experimentally measured velocity at the wall to zero. The experimental non-dimensional boundary layer profiles at 5 and 10 [m/s] free stream velocity are very similar. However, these boundary layers have a less full profile than the theoretical flat plate boundary layer. This is caused by the slight unfavourable pressure gradient induced

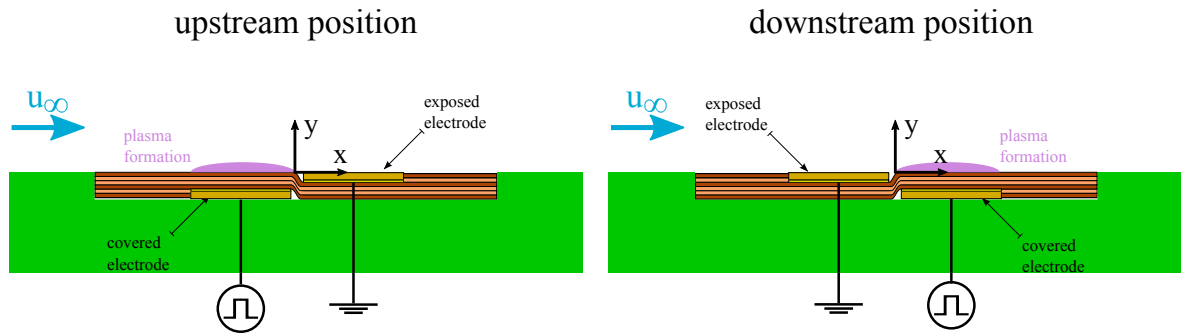


Figure 5.1: Schematic representation of the streamwise positioning of the covered HV electrode. Different scaling is used for x- and y-direction for better clarity.

by the elliptical leading edge of the wind tunnel model. The shape factor underlines the presence of a laminar boundary layer by the similarity to the laminar Blasius profile.

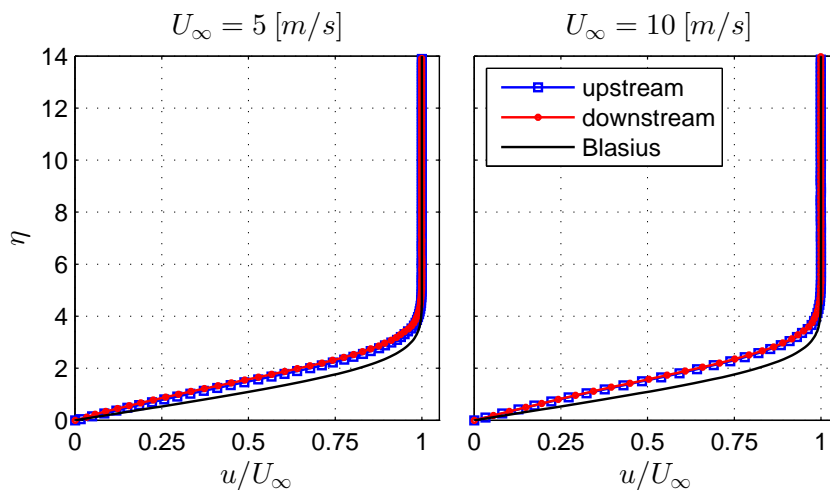


Figure 5.2: The non-dimensional u-velocity boundary layer profile both at $U_\infty = 5$ [m/s] and 10 [m/s], with the flat surface of the model parallel to the freestream.

Table 5.1: Shape factor (H) of the boundary layer profiles shown in figure 5.2. Upstream and downstream correspond to the position of the covered HV electrode position of the ns-DBD plasma actuator.

Profile	Freestream velocity	
	5 [m/s]	10 [m/s]
Upstream	2.83	2.86
Downstream	2.94	2.88
Blasius	2.59	2.59

5.2.2 Disturbance by ns-DBD in a laminar boundary layer

The velocity field disturbance introduced by the tested ns-DBD plasma actuator is visualized by the difference (V') between the velocity field after discharge (V_{dis}) and the undisturbed flow conditions (V_0), thus by $V' = V_{dis} - V_0$. This similar difference is used to visualize the separate u' and v' components.

The relation of the velocity field disturbance, expressed in u-velocity difference (u'), with energy input is shown in figure 5.3. Additionally, the growth of the v-velocity difference (v'), combined with the disturbed vector field (V') is shown in figure 5.4. These results are shown 0 [ms] after the discharge burst for both upstream and downstream position of the covered HV electrode. A strong relation in flow disturbance depending on the streamwise position of the covered HV electrode of the ns-DBD plasma actuator is present. Moreover, a growth of the disturbed velocity field area is visible with increased energy input.

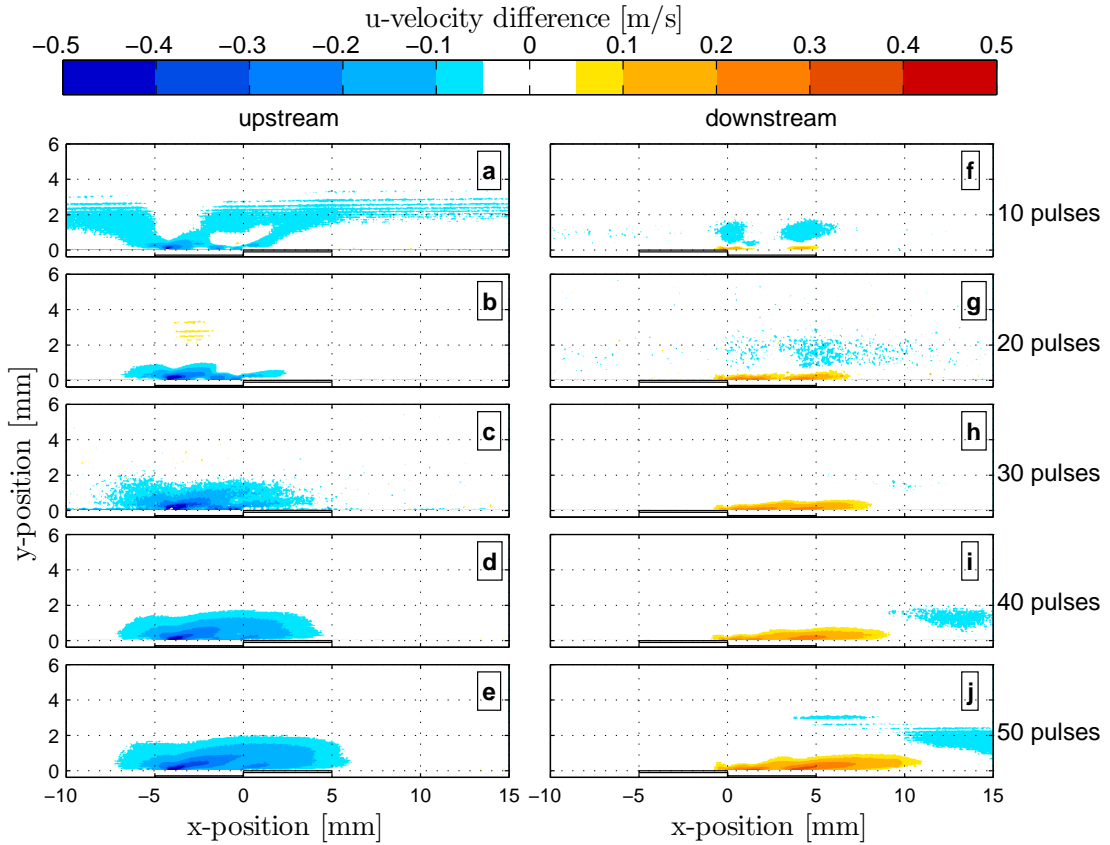


Figure 5.3: Disturbance growth in u-velocity difference (u') for both up and downstream position of the covered HV electrode in a laminar boundary layer with a 5 [m/s] freestream. Results acquired 0 [ms] after of a burst of 10 – 50 pulses of 10 [kV] at 10 [kHz].

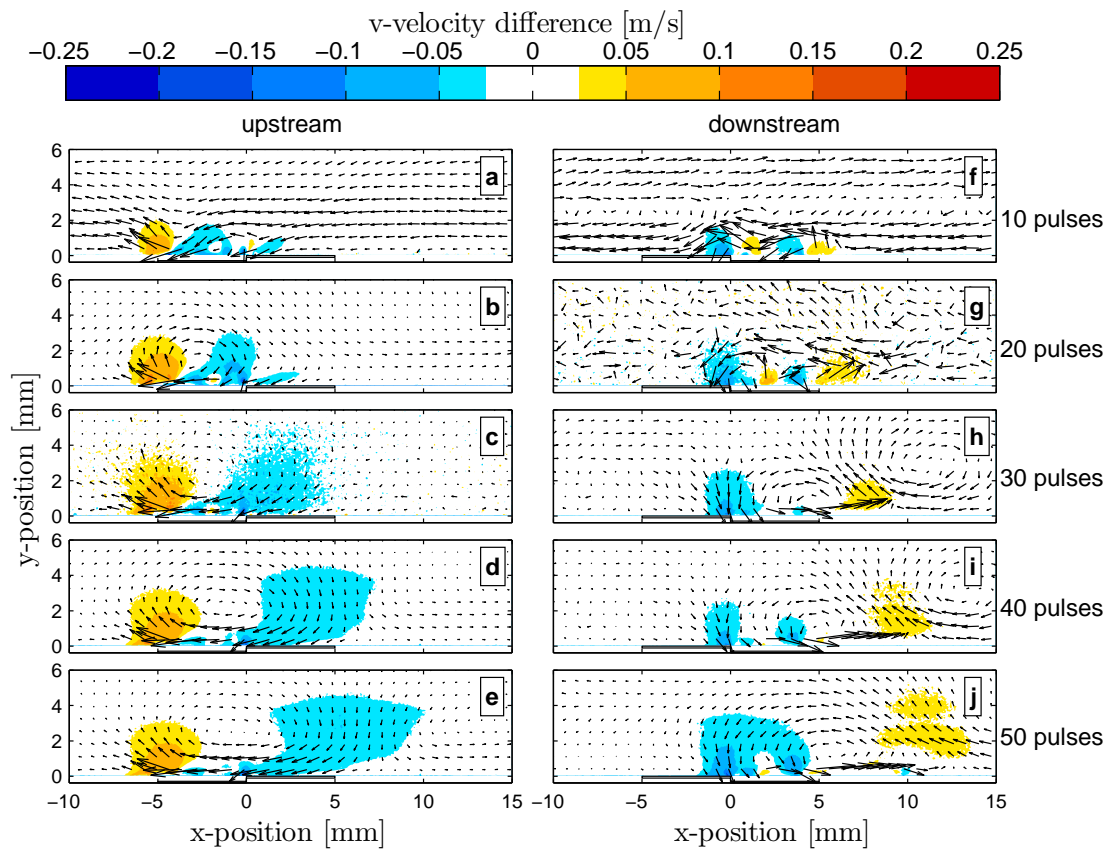


Figure 5.4: Disturbance growth shown in contours of v' , with vector components (V') in both up and downstream position of the covered HV electrode. Disturbance in a laminar boundary layer with a $5 [m/s]$ freestream. Results acquired $0 [ms]$ after of a burst of $10 - 50$ pulses of $10 [kV]$ at $10 [kHz]$.

Figures 5.3.a-e show that an ns-DBD plasma actuator with an upstream positioned covered HV electrode induces a deceleration of the near wall volume of air. This deceleration has maximum value between -0.4 and -0.55 [m/s], as shown in figure 5.5. For the energy input of 50 pulses this results in a mean local velocity (u) of 0.09 [m/s] in the discharge region, which is taken between $x = -5$ to 0 [mm] and $y = 0$ to 0.25 [mm]. The energy input of 20 pulses (figure 5.3.b) produces a stronger local acceleration above the decelerated near wall volume, which is not visible with the same magnitude in the results of the other cases. Next to this, the result for a discharge burst of 10 pulses in figure 5.3.a shows a significantly larger size and structure of local deceleration than the other results (figure 5.3.b-e). This is due to a slightly larger error between freestream velocity (u_∞) of the disturbed velocity field (u_{dis}) and undisturbed velocity field (u_0) compared to the other results. A list of freestream velocity errors between the undisturbed and disturbed velocities is shown in table 5.2. When the vector field (V') results and v-velocity difference (v') contours in figure 5.4.a-e are considered, it is evident that the application of 20 (or more) discharge pulses leads to the formation of a vortex like structured disturbance. This vortex like disturbance is in clockwise direction, with the rotational-center moving downstream with the application of more pulses. A counter-clockwise rotating vortex like structure appears to be induced downstream of the original structure when more than 40 discharge pulses are applied (figures 5.4.d-e).

Figures 5.3.f-j show that an ns-DBD plasma actuator with a downstream positioned covered HV electrode produces an acceleration of the near wall volume of air. This local acceleration reaches a maximum velocity difference (u') between 0.27 and 0.4 [m/s] as shown in figure 5.5. For the energy input of 50 pulses this results in a mean local velocity (u) of 0.55 [m/s] in the discharge region, taken between $x = -5$ to 0 [mm] and $y = 0$ to 0.25 [mm]. The evolution shown in figure 5.3.f-j indicates two local accelerations, starting at $x = 0$ and 4 [mm], which grow with energy input. These separate accelerations merge when more than 20 pulses are applied. The maximum induced accelerated velocity (u') is also lower when the two separate zones are merged. The deceleration zone above the accelerated near wall volume is less pronounced with more energy input and appears to move downstream. The total area of disturbance in u' component is approximately 1 [mm] height, which is about half of that of the deceleration zone in the other electrode orientation. When the the vector field (V') and v-velocity difference (u') contours in figure 5.4.f-j are considered, it is evident that a downstream positioned covered HV electrode also introduces a vortex like disturbance. The vector fields for 10 and 20 pulses (figures 5.4.f-g) are noisy due to a mismatch between undisturbed and disturbed freestream velocities and small velocity differences. However, the combination of the separate u' (figures 5.3.f-g) and v' components (figures 5.4.f-g) indicates two counter-clockwise rotating vortex structures close to wall. When more than 30 pulses are applied these separate structures merge to form one larger counter-clockwise rotating disturbance. On its own, this disturbance induces a clockwise rotating vortex like structure downstream of the original structure.

The absolute values of induced velocity shown in figure 5.5 are slightly lower than the 0.5 [m/s] measured in experiments by [Little et al. \(2012\)](#). The differences could originate from the fact that [Little et al. \(2012\)](#) used a 30 [kV] input signal at 2 [kHz], while present results are created with a 10 [kV] input signal at 10 [kHz]. However, the induced velocity results indicate the presence of a small electrohydrodynamic (EHD) force, which is directed from the grounded exposed to the covered HV electrode. The superposition of the undisturbed flow and the

resulting near wall directional acceleration leads to the formation of vortex like structure in the disturbed velocity field. This vortex like structure in the disturbed velocity field (V') is not to be confused with the formation of a vortex in the measured velocity field (V). However, the vortex like disturbance induces a vertical velocity component which mixes the air at different heights within the boundary layer with each other. Additionally, the local deceleration in u' component modifies the shape of the boundary layer, creating an inflection point that destabilizes the boundary layer. This makes the boundary layer more susceptible to natural flow instabilities, which implies that these instabilities can grow within the boundary layer. The local acceleration in u' component creates a fuller laminar boundary layer profile, which would imply stabilization of said boundary layer. However the presence of a vortex like disturbance still adds vertical movement within the boundary layer. This vertical component was also visible downstream of the actuator in PIV results of [Correale et al. \(2014\)](#). Those results indicated the presence of a Tollmien-Schlichting wave downstream of the discharge zone.

Table 5.2: Error in freestream u-velocity (u') between undisturbed and disturbed boundary layer flow at $y = 5.5 - 6.0$ [mm] from the wall.

Freestream velocity	Energy input	Error in freestream velocity, for covered HV electrode position;	
		upstream	downstream
5[m/s]	10 pulses	-0.0245 [m/s]	0.0187 [m/s]
	20 pulses	0.0100 [m/s]	-0.0115 [m/s]
	30 pulses	0.0016 [m/s]	0.0076 [m/s]
	40 pulses	0.0131 [m/s]	0.0028 [m/s]
	50 pulses	0.0025 [m/s]	-0.0197 [m/s]
10[m/s]	50 pulses	0.0004 [m/s]	0.0042 [m/s]

In figure 5.5 the maximum absolute values of the u-velocity disturbance (u') are shown as a relation to the energy input (in pulses). These values are measured between $x = -10$ and 10 [mm] at a height between $y = 0$ and 2 [mm]. Outliers due to reflections or other optical aberrations are neglected. The magnitude of the results of the downstream cases is larger for the upstream case than for the downstream case at all energy inputs. Since the ns-DBD plasma actuator is of equal construction in both cases, and similar energy is used per pulse, the assumption is made the body force should be of similar magnitude. Therefore, a second flow effect should be present which slows the flow down. As shown in section 2.1, an increase in temperature will increase the dynamic viscosity (μ) in gas. If the discharge of the ns-DBD plasma actuator produces more heat at the wall then away from the wall, a negative temperature gradient ($\partial T/\partial y|_{y=0}$) is created. Therefore, due to proportionality in gas, a negative viscosity gradient at the wall ($\partial \mu/\partial y|_{y=0}$) is then present. Moreover, this decelerates the local boundary layer. Overall, this results in more local deceleration of the flow when coupled to a body force in flow opposite direction (upstream case) and less acceleration of the flow when coupled to a body force in flow-wise direction (downstream case).

The effect of the freestream velocity on the disturbance of a discharge burst of 50 pulses is shown in figures 5.6 and 5.7. The disturbance is stretched out in streamwise direction in

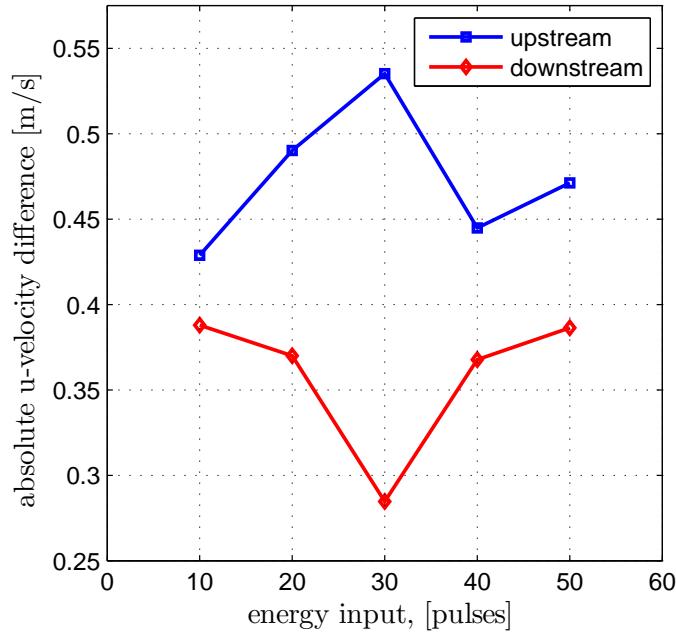


Figure 5.5: Maximum absolute u-velocity (u') disturbance introduced by the ns-DBD plasma actuator in a laminar boundary layer with 5 [m/s] freestream. Values for upstream indicate a deceleration, those for downstream indicate an acceleration.

the 10 [m/s] freestream (figure 5.6) relative to the 5 [m/s] freestream (figure 5.7). The total length of the decelerated area is approximately 25 [mm] in the 10 [m/s] case, which is twice as large as the 12.5 [mm] in the 5 [m/s] case. However, the disturbance has approximately the same height compared to the 5 [m/s] freestream case, thus 2 [mm] for upstream and 1 [mm] for downstream positioning of the covered HV electrode. The maximum deceleration by then ns-DBD plasma actuator in with upstream positioned covered HV electrode is reduced in absolute magnitude to -0.44 [m/s]. For the downstream positioned covered HV electrode the maximum local acceleration is 0.47 [m/s].

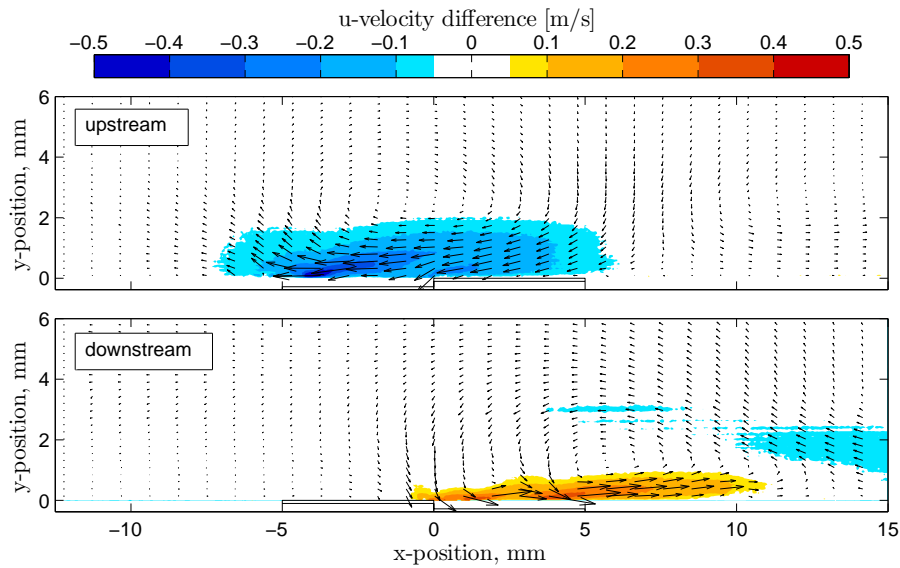


Figure 5.6: Disturbance in u -velocity difference (u') with vector components (V') for both up and downstream position of the covered HV electrode in a $5 [m/s]$ freestream. Results acquired $0 [ms]$ after of a burst of 50 pulses of $10 [kV]$ at $10 [kHz]$.

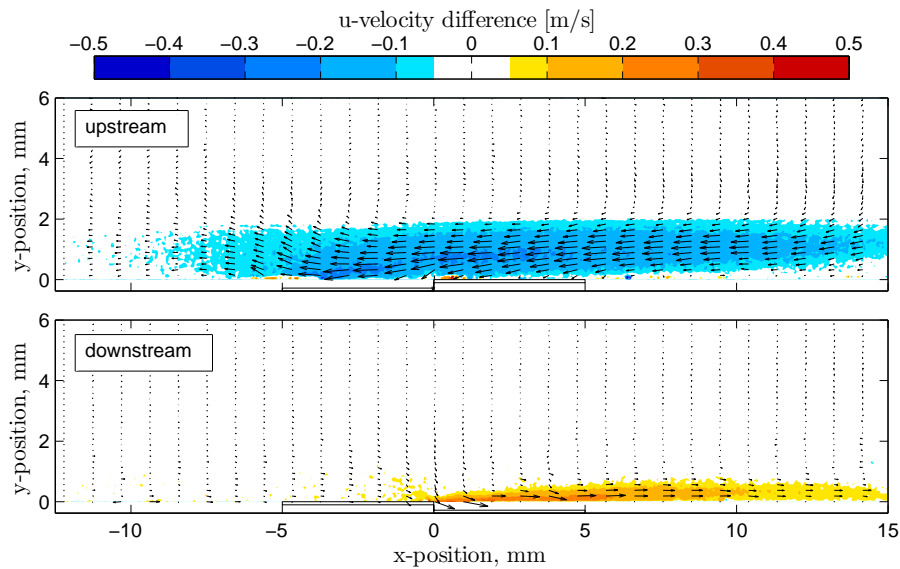


Figure 5.7: Disturbance in u -velocity difference (u') with vector components (V') for both up and downstream position of the covered HV electrode in a $10 [m/s]$ freestream. Results acquired $0 [ms]$ after of a burst of 50 pulses of $10 [kV]$ at $10 [kHz]$.

5.3 Energy measurements

The energy usage per discharge pulse of the ns-DBD plasma actuator is measured for both streamwise positions of the covered HV electrode. For a good comparison of the flow effects the energy usage of both geometrical orientations should be equal. Figure 5.8 shows for both the upstream and downstream position of the covered HV electrode the measured voltage evolution over time. This is the voltage trace for the first pulse of the burst of 50 pulses of which the flow effect was shown in figure 5.6.

The results indicate that the voltage trace is very similar for both cases. A breakdown of the energy input (E_{in}), output (E_{out}) and energy per pulse used by the actuator system (E_{pp}) is shown in table 5.3. This indicates that the amount of energy deposited to the air and dissipated internally in the actuator system is $15.25 [mJ/pulse]$ for upstream and $14.87 [mJ/pulse]$ for downstream positioning of the covered HV electrode. Separation between energy deposition to the air and dissipated in the system is at the moment not possible. However, since the same actuator is used for both streamwise positions of the covered HV electrode the fraction of thermal energy deposition to the flow should be similar as well. Furthermore, it is assumed that discharge pulses are repeatable because thermal energy deposition per discharge pulse was shown by the volumetric heating in section 4.4.

Figures 4.9 and 5.8 indicate a big difference in the voltage trace. The reflected pulse is completely downstream in figure 4.9, but has both a positive and negative component in figure 5.8. The only geometrical differences between both measurements are the thickness of the barrier and the length of the electrodes. Therefore the discharge strength and discharge length can be at cause for the reflection, doubling and reversal of the measured voltage. However, this makes no difference for the calculated energy.

Table 5.3: Energy per pulse (E_{pp}) for the both upstream and downstream positioning of the covered HV electrode.

Energy	Covered HV electrode position:	
	upstream	downstream
$E_{in} [mJ]$	21.76	21.63
$E_{out} [mJ]$	6.51	6.76
$E_{pp} [mJ]$	15.25	14.87

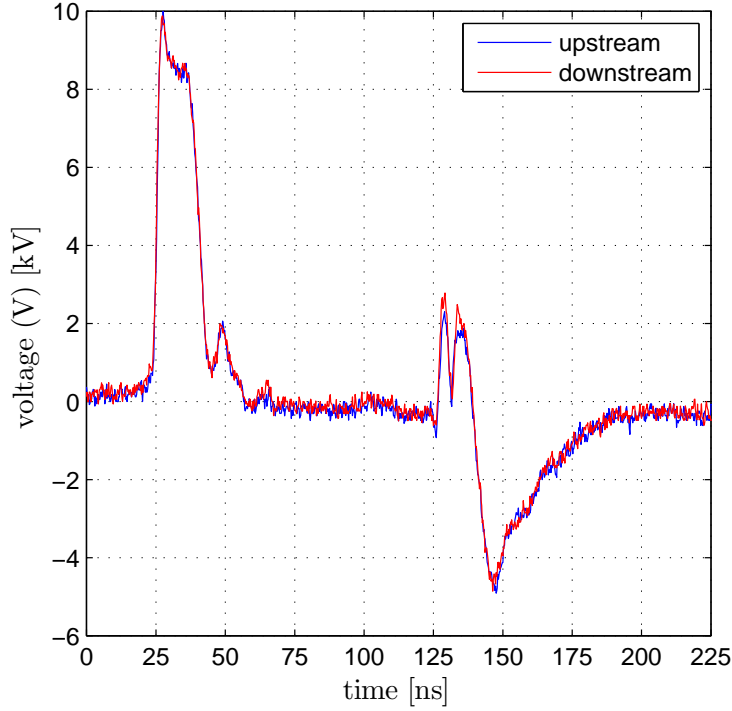


Figure 5.8: Voltage over time for the first pulse of a burst of 50 pulses at 10 [kV] and 10 [kHz] for the ns-DBD plasma actuator with the covered electrode in both streamwise positions.

5.4 Density method validation and results

The theory to calculate the density field from the compressible mass continuity equation (section 5.1) is used here to quantify the density fields associated with the velocity fields disturbances shown in figure 5.3.

Pre-processing of the experimentally measured velocity fields is needed to ensure that the finite difference method used does not experience exponential growth due to large velocity field gradients. The velocity field under the influence of plasma discharge (V_{dis}) is smoothed out with a two dimensional Gaussian smoothing filter. This filter is set to a radius (R) of 10 velocity vector field indices and standard deviation (σ) of 3 indices. Velocity field results closer to the wall are susceptible to measurement artefact's which are removed with an additional one-dimensional filter in stream wise direction with a weighted linear squares model. This filter was given a span of 100 velocity vector field indices at the first row of indices above the wall, reduced with steps of 10 to 0 at the tenth row of velocity field indices above the wall. All these settings are determined such to avoid exponential growth in the Finite Difference calculation. Initial and boundary conditions are set to the undisturbed density at sea level ($\rho_0 = 1.225 [kg/m^3]$). Moreover, it should be mentioned that the complete disturbed velocity

field (V_{dis}) is used for these calculations, not the previously displayed velocity difference fields (V').

Validation of the proposed density calculation is at the moment only possible with data from previously conducted Schlieren experiments by [Correale et al. \(2014\)](#). In these experiments the disturbance of a ns-DBD plasma actuator in a laminar boundary layer has been recorded with Schlieren imagery. The experimental conditions in these experiments are similar to the testing conditions in this thesis; a 5 [m/s] freestream velocity, a discharge burst 50 pulses at 10 [kV] and 10 [kHz] with the covered HV electrode in upstream position. From the determined perturbed density field by the proposed method, the density gradient in wall normal direction is determined (resulting in synthetic Schlieren). This is compared to the corresponding density gradient visualized by experimental time resolved Schlieren. Figure 5.9 shows that at 5 [m/s] freestream conditions, the results have a similar structure in the density gradient field to the validation data. However, the synthetic Schlieren results show more oscillations emanating from the wall. These are caused by the abbreviations in the measured velocity field near the wall, which are smoothed, thereby spreading over a larger area. From the results of the 10 [m/s] freestream conditions it can be observed that a large difference exists between validation and synthetic Schlieren images. The disturbed structure in the synthetic Schlieren is about twice as low as the Schlieren result of the validation data. A possible explanation for this is shown in figure 5.10. These images show the result for the incompressible continuity equation for the undisturbed flow, and the flow disturbed by a discharge burst of 50 pulses, both with the covered HV electrode in upstream position. The incompressible continuity equation is a primary part of the discretized compressible continuity equation shown in equation 5.2. These results indicate that the continuity condition is not satisfied for the smoothed velocity vector fields of the undisturbed flow. Moreover, the disturbance structure observed for the disturbed flow of 10 [m/s] has a lower height, than the structure in the disturbed flow of 5 [m/s] freestream. This is a possible result of the smoothing applied to vector fields, which has a different effect on the 10 [m/s] freestream flow with higher convection compared to the 5 [m/s].

Calculated results are visually validated based on structure as previously demonstrated by [Opaits et al. \(2008\)](#). The perturbed density gradient field at 5 [m/s] is concluded to give a good representation of the experimental density field, although not without flaws when applied at 10 [m/s].

Figure 5.11 shows the phase locked perturbation with respect to the initial density field in percentage dependent on energy input per burst for both upstream and downstream stream wise position of the covered HV electrode. The aforementioned velocity difference fields showed a directional difference with upstream and downstream covered HV electrode position, but the density field has a similar structure for upstream and downstream position. Independent on the covered HV electrode position and corresponding induced velocity field (V') the effect of discharge is a decrease in local density (ρ) with respect to the initial density field (ρ_0). It is observed that an increase in pulses (thus energy deposition) induces a decrease in local density, as observed in the Schlieren experiments in section 4.4. An upward limit for energy deposition is not observed within this experiment. Oscillations between density increase and decrease near the wall are accredited to aforementioned aberrations in the measured velocity vector fields at locations with reflections at the wall.

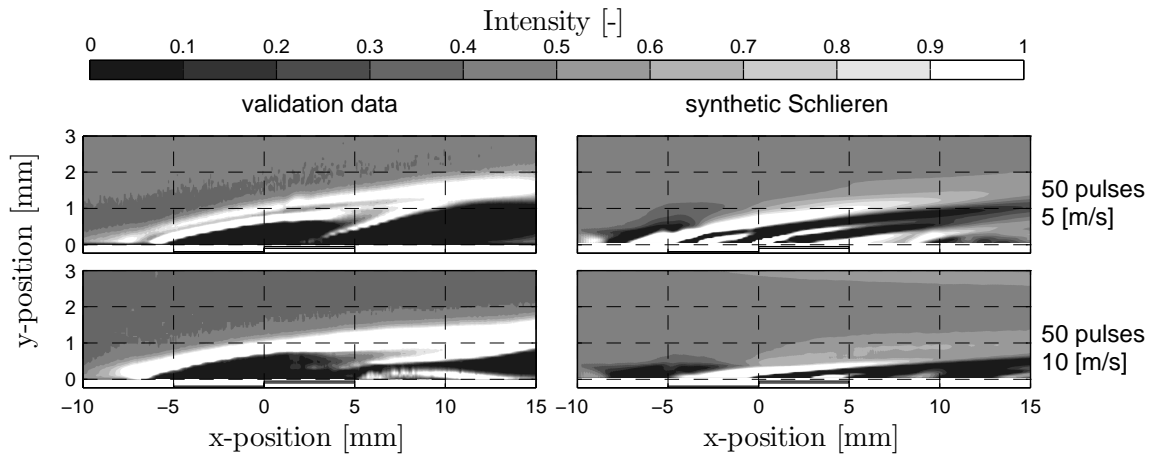


Figure 5.9: Comparison of the validation data with the calculated density gradient in wall normal direction (synthetic Schlieren). Covered HV electrode in upstream position for both experiments, while the actuator is fed with a 10 [kV] signal at 10 [kHz]. Different scaling is used for x- and y-direction for better clarity.

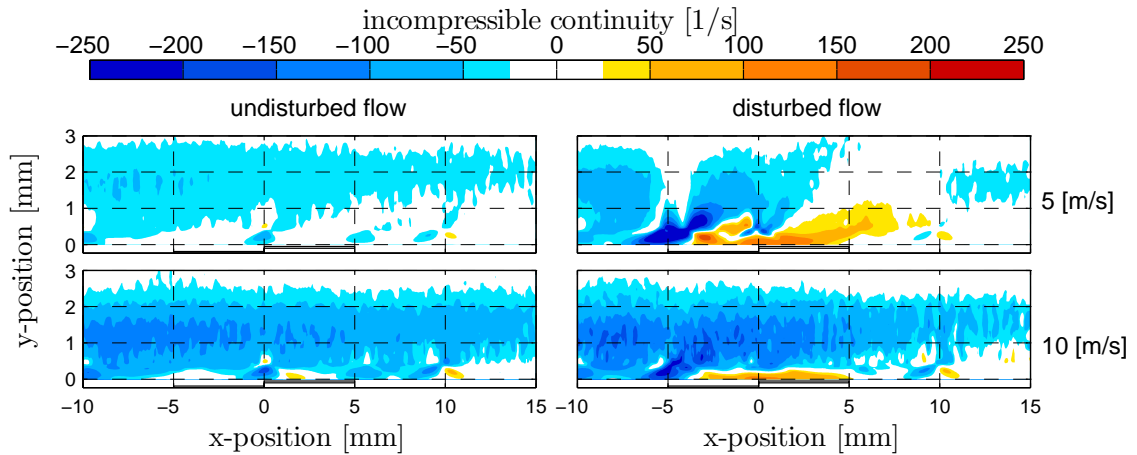


Figure 5.10: Value of the incompressible continuity equation for the case with the covered HV electrode in upstream position with a 10 [kV] signal at 10 [kHz]. Different scaling is used for x- and y-direction for better clarity.

Measured velocity fields indicated a mean velocity (u) of $0.09 [m/s]$ over covered HV electrode in upstream position and $0.55 [m/s]$ for the downstream position. A lower velocity implies that air particles will have a longer residence time in the by plasma heated area. A larger temperature increase is thereby expected. However, results in figure 5.11 indicate primarily a larger area of density decrease than a larger magnitude of density decrease for the upstream position relative to the downstream position. A reason for this might be that the ns-DBD

plasma actuator with a downstream positioned covered HV electrode draws colder air to the discharge zone and convects this at higher velocity past the wall of the model. This allows more heat to be absorbed and dissipated by the wall.

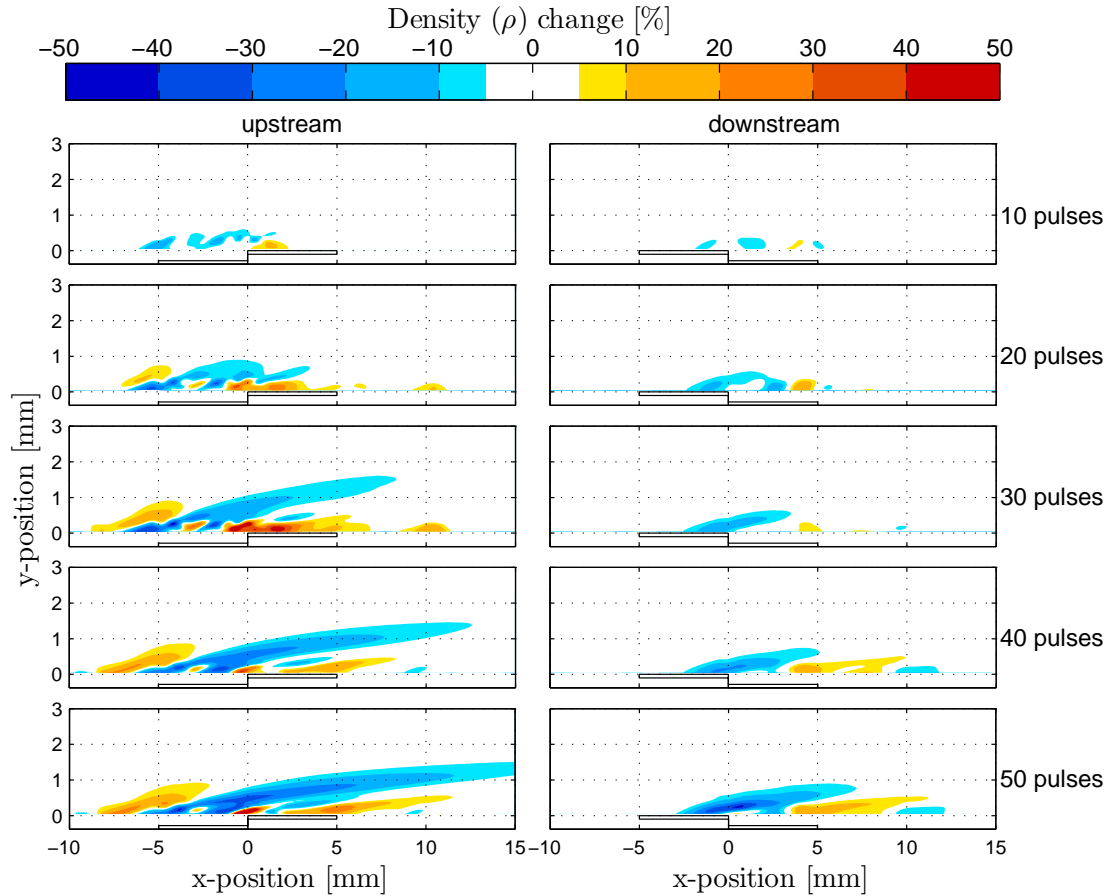


Figure 5.11: Perturbation with respect to the initial density field ($\rho_0 = 1.225 [kg/m^3]$) in percentages. Results for the measured flow field disturbances 0 [ms] after a burst of 10 – 50 pulses at 10 [kV] and 10 [kHz] for both upstream and downstream positioning of the HV covered electrode. Different scaling is used for x- and y-direction for better clarity.

5.5 Discussion

The results of the PIV experimental investigation into the laminar boundary layer flow disturbance by the tested ns-DBD plasma actuator are discussed in this section. Focus of this investigation was on the velocity field disturbance, energy usage of the actuator and the calculated density field change due to plasma discharge.

- Measured velocity field disturbances have indicated that a dependence on the streamwise positioning of the covered high voltage electrode is present during ns-DBD plasma actuator discharge in a laminar boundary layer. The local acceleration of the boundary layer by downstream position and deceleration by the upstream position of the covered HV electrode indicates the presence a small body force. This body force is directed from the grounded exposed to the covered HV electrode. The maximum absolute perturbation velocity (u') is slightly lower than values measured by [Little et al. \(2012\)](#). Superposition of the undisturbed flow and small local accelerations/decelerations provoke the formation of a vortex like disturbance in the perturbation velocity V' . It is important to understand that these are not vortices in the measured velocity field V , thus no local reversed flow ($u < 0$) is present in the results. However, the local vortex like disturbance introduces a vertical velocity (v') which improves mixing of air at various heights in the boundary layer. Furthermore, an increase in energy input results in a larger area of velocity field disturbance.
- The magnitude of the local acceleration (downstream case) is lower then to the deceleration (upstream case) at equal energy input. The body force is assumed of similar magnitude (but in opposite direction), due to its equal construction but opposite positioning. Therefore, the magnitude difference can be explained with the combination of the body force and an increased dynamic viscosity (μ) at the wall. The temperature and viscosity gradients are proportional as shown in section 2.1. Furthermore, if due to the plasma discharge the air temperature is higher at the wall then away from the wall, a negative viscosity gradient at the wall will be created. This decelerates the flow at the wall. The combination of these effects results in a net larger deceleration magnitude in the upstream case, compared to the acceleration magnitude in the downstream case.
- Measured energy associated with one discharge pulse of the tested actuator system was shown to be very similar for both streamwise positions of the covered HV electrode.
- Quantification of the density field perturbation with the discretized compressible mass continuity equation was validated with Schlieren results. This validation showed that a reasonable approximation is given under the tested conditions, but not without errors. Phase-locked density field perturbation with respect to the initial density field indicates that more energy input results in a larger area of density field disturbance. Additionally, the results showed that the ns-DBD plasma actuator with an upstream positioned covered HV electrode affects a larger area than with a downstream positioned covered HV electrode. Similar energy was used in the discharge of both streamwise positions, which indicates that the the flow field induced plays and important role in thermal energy distribution. This underlines that while the thermal deposition is a dominant factor in the flow coupling mechanism, geometrical construction of the actuator with respect to the streamwise direction can enhance the effect by increased mixing.

Conclusions and Recommendations

6.1 Conclusions

The aim of this study was to understand the influence of the barrier of an ns-DBD plasma actuator on the energy deposition to the near wall volume of air. In addition, the direct effect of energy deposition by a ns-DBD plasma actuator on a laminar boundary layer was investigated.

The density field disturbance in quiescent conditions by an ns-DBD plasma actuator fed with bursts of pulses at $10 [kHz]$ and $10 [kV]$ was determined with the use of Schlieren imagery and quantified in disturbed area. Barriers of the tested ns-DBD plasma actuator were made out of Kapton[®] Polyimide tape, silicone-rubber or Fine Polyamide PA2200, with each barrier material tested at several thicknesses. Energy measurements were made with a back-current shunt placed within the high voltage coaxial cable which connected the power generator with the plasma actuator. Results indicated that:

- Disturbed density fields by thermal energy deposition of the plasma discharge showed that the structure of the disturbance is dependent on the barrier material. Moreover, the ns-DBD plasma actuators with a silicone-rubber or PA2200 barrier have a secondary discharge on the opposite side of the exposed electrode relative to the covered electrode position. This is due to their lower volume resistivity (ρ_{vr}) relative to a Kapton barrier. Due to the porosity of the PA2200 barrier, a more filamentary and brighter discharge is present than in an ns-DBD plasma actuator with Kapton or silicone-rubber barrier.
- As with earlier experiments by [Michelis et al. \(2013\)](#) and [Correale et al. \(2014\)](#) a linear increase of disturbed area while discharge is on is observed for the barrier made out of Kapton. However, if more than 100 pulses per burst at $10 [kHz]$ and $10 [kV]$ are applied thermal expansion and buoyancy effects become dominant, reducing the area calculation capabilities. The linear trend is also visible in the results of silicone-rubber and PA2200.
- With equal applied voltage signal, an ns-DBD plasma actuator with a thinner barrier

of the same material deposits more thermal energy per pulse to the near wall volume of air than one with a thicker barrier. This is due to the lower distance between the two electrodes, resulting in a higher reduced electric field strength and stronger thermal deposition through dissociation of air particles.

- The tested actuators with a Kapton barrier produce a larger density field disturbance than these with a silicone-rubber barrier, which in turn disturb a larger area than those with a PA2200 barrier. Thermal expansion of the heated area after discharge is dependent on the barrier material as well. Similar thermal conductivity of the Kapton and silicone-rubber barriers implies that the sharp decrease in disturbed area after discharge might be a function of the heat capacity of the barrier. Both the Silicone-rubber and PA2200 barriers have a larger volume to which heat can be dissipated. The porous structure of the PA2200 barrier results in a lower thermal conductivity and a slower rate of thermal energy absorption.

It can be concluded that a barrier in an ns-DBD plasma actuator should have a low thickness, high electrical volume resistivity, low thermal capacitance and low heat capacity in order to efficiently deposit thermal energy to the nearby air.

The disturbance of an ns-DBD plasma actuator with a barrier made out of 2 layers of Kapton tape in a laminar boundary layer was investigated with phase-locked planar Particle Image Velocimetry (PIV). Velocity field disturbances, back-current shunt energy measurements and density calculations revealed that:

- A strong dependence on the streamwise orientation of the electrodes of the ns-DBD plasma actuator is present with respect to the disturbance introduced into the laminar boundary layer. An ns-DBD plasma actuator with the covered high voltage electrode in upstream position decelerates the near wall volume above the covered electrode while a downstream positioned covered HV electrode accelerates the flow. The absolute amplitudes of these disturbances are between 0.3 and 0.5 [m/s], which is slightly lower than found in experiments by [Little et al. \(2012\)](#). Moreover, these disturbances indicate the presence of a small body force directed from the grounded exposed to the high voltage covered electrode. The local accelerations/decelerations provoke the formation of a vortex like disturbance in the perturbation velocity fields. These are not vortices in the measured velocity field. However, they do introduce a local vertical velocity component which improves mixing of the air from various heights within the boundary layer. Furthermore, differences between the magnitude of deceleration and accelerations are accredited to the induced viscosity gradient at the wall. This reduces the near wall velocity, resulting in an extra deceleration in the upstream case and less acceleration in the downstream case.
- A method of quantifying the disturbed density field by a backward-time backward-space finite difference approximation of the compressible continuity equation was proposed. It was validated and shown to give a reasonable physical indication of the density field disturbance under the tested conditions. The method is not without flaws, however, it is able to quantify density changes through less separate steps and assumptions than current calculations through CFD solvers.
- Independent on streamwise orientation of the actuator geometry the effect of discharge

is always a decrease of local density value and an increase of affected density field area with increased energy input. The affected area of density field change with respect to the initial density field is larger in the case of an upstream positioned covered high voltage electrode than for a downstream positioned one. However, energy measurements showed that similar energy was deposited in both streamwise orientations. This indicates that the velocity field plays a role in the thermal energy coupling to the laminar boundary layer.

To conclude, this study was able to indicate that the streamwise orientation of the ns-DBD plasma actuator can enhance the mixing of the thermal energy deposition in the near wall volume of air. Directing the produced body force in opposite direction to the freestream flow, induces a velocity field disturbance which appears to increase the transport of the thermal energy deposition in the boundary layer.

6.2 Recommendations

During the experiments, post-processing and the formation of the conclusions a few recommendations for future research arose:

- Barrier materials with accurate specifications regarding electrical and heat dissipation characteristics are preferred. More focus can then be given to the effects of these barriers on the discharge rather than on designing and exploring measurement techniques to determine the material specifications.
- The small drift over time in the freestream velocity of the windtunnel creates a small error in the calculated velocity difference fields (u'). Another testing procedure is proposed. Instead of acquiring 300 phase-locked image pairs of undisturbed flow, followed by 300 phase-locked image pairs of disturbed flow, new tests could be made with only one set of 600 phase-locked image pairs. This set would then contain one undisturbed image pair, followed by one disturbed image pair, and so on. In this way, the same drift in freestream velocity is present in the Sum-of-Correlation results of the disturbed and undisturbed set.
- The original back-current shunt calibration process was not successful and should be corrected for future energy measurements. In this way the results can be compared to other academic results.
- The current study was able to give a quantification of the density field changes by ns-DBD plasma discharge in the laminar boundary layer. However, the change in viscosity is not yet quantified, while [Lecordier et al. \(2000\)](#) considered this change more important than the change in density during his experiments. The value for dynamic viscosity (μ) could be calculated through the Sutherland relation if the temperature in the boundary layer could be quantified. This is in practice difficult to do. Additionally, usage of the compressible momentum equation can be considered. However, the combination of changes in density, changes in viscosity and the presence of a local body force introduces a difficulty in solving the equation for the viscosity. A simplification of the equations

can be made with the assumption of equal magnitude but opposite direction of the body force in both investigated cases. Next to this, pulses are considered repeatable and the discharge burst is seen as an instant effect by the flow.

- A direct comparison between an ns-DBD plasma actuator and a pulsed wall or near-wall-volume heating device will increase the understanding of the importance of the small body force with respect to the thermal energy deposition for the flow control capabilities of said actuators.
- Separation between thermal energy deposition to the near wall volume of air and electrical and thermal energy dissipation in the barrier would improve the conclusions of barrier optimization studies. Next to this, better knowledge of the energy deposition to the near-wall volume of air would provide better validation or input data for the (in the previous point) proposed experiment.

Bibliography

- A. Aba'a Ndong, N. Zouzou, N. Benard, and E. Moreau. Effect of dielectric aging on the behavior of a surface nanosecond pulsed dielectric barrier discharge. *IEEE Trans. Dielectr. Electr. Insul.*, 20(5):1554–1560, oct 2013. ISSN 1070-9878. doi: 10.1109/TDEI.2013.6633683. URL <http://www.scopus.com/inward/record.url?eid=2-s2.0-84887036876&partnerID=tZ0tx3y1>.
- N L Aleksandrov, S V Kindysheva, M M Nudnova, and A Yu Starikovskiy. Mechanism of ultra-fast heating in a non-equilibrium weakly ionized air discharge plasma in high electric fields. *J. Phys. D. Appl. Phys.*, 43(25):255201, jun 2010. ISSN 0022-3727. doi: 10.1088/0022-3727/43/25/255201. URL <http://www.scopus.com/inward/record.url?eid=2-s2.0-77953549927&partnerID=tZ0tx3y1>.
- N. Benard, N. Zouzou, A. Claverie, J. Sotton, and E. Moreau. Optical visualization and electrical characterization of fast-rising pulsed dielectric barrier discharge for airflow control applications. *Journal of Applied Physics*, 111(3), 2012. doi: 10.1063/1.3682568. URL <http://www.scopus.com/inward/record.url?eid=2-s2.0-84857434888&partnerID=40&md5=a1a18e28d52ec6065fe606c02fded0af>.
- A.V. Berdushev. Molecular Gas Heating in Pulsed MW Discharge. *High Temperature (Teplofizika Vysokikh Temperatur)*, Volume 26(4):661–666, 1988.
- J. P. Boeuf and E. E. Kunhardt. Energy balance in a nonequilibrium weakly ionized nitrogen discharge. *J. Appl. Phys.*, 60(3):915, 1986. ISSN 00218979. doi: 10.1063/1.337332. URL <http://link.aip.org/link/JAPIAU/v60/i3/p915/s1&Agg=doi>.
- L.N. Cattafesta and M. Sheplak. Actuators for Active Flow Control. *Annu. Rev. Fluid Mech.*, 43(1):247–272, jan 2011. ISSN 0066-4189. doi: 10.1146/annurev-fluid-122109-160634. URL <http://www.scopus.com/inward/record.url?eid=2-s2.0-79951966911&partnerID=tZ0tx3y1>.
- T.C. Corke, M.L. Post, and D.M. Orlov. Single dielectric barrier discharge plasma enhanced aerodynamics: physics, modeling and applications. *Experiments in Fluids*, 46(1):1–26, nov 2009. ISSN 0723-4864. doi: 10.1007/s00348-008-0582-5. URL <http://www.scopus.com/inward/record.url?eid=2-s2.0-57849169323&partnerID=tZ0tx3y1>.
- T.C. Corke, C. L. Enloe, and S P. Wilkinson. Dielectric Barrier Discharge Plasma Actuators for Flow Control. *Annu. Rev. Fluid Mech.*, 42(1):505–529, jan 2010. ISSN 0066-4189. doi:

- 10.1146/annurev-fluid-121108-145550. URL <http://www.scopus.com/inward/record.url?eid=2-s2.0-77952830330&partnerID=tZ0tx3y1>.
- G Correale, I.B. Popov, A.E. Rakitin, A. Yu. Starikovskii, Hulshoff. S.J., and L.L.M Veldhuis. Flow separation control on airfoil with pulsed nanosecond discharge actuator. In *49th AIAA Aerosp. Sci. Meet. Incl. New Horizons Forum Aerosp. Expo. 2011*, 2011.
- G. Correale, T. Michelis, D. Ragni, M. Kotsonis, and F. Scarano. Nanosecond-pulsed plasma actuation in quiescent air and laminar boundary layer. *Journal of Physics D: Applied Physics*, 47(10), 2014. doi: 10.1088/0022-3727/47/10/105201. URL <http://www.scopus.com/inward/record.url?eid=2-s2.0-84894434815&partnerID=40&md5=5087673e6c708b3192f5792bbdf5fe11>.
- G. Correale, R Winkel, and M Kotsonis. Energy deposition characteristics of ns-DBD plasma actuators: influence of dielectric material (under review). *Journal of Physics D: Applied Physics*, 2015.
- N. S. Dougherty and D. F. Fisher. Boundary-layer transition on a 10-deg cone: wind tunnel/flight correlation. In *AIAA Pap.* AIAA, 1980. URL <http://www.scopus.com/inward/record.url?eid=2-s2.0-0019248355&partnerID=tZ0tx3y1>.
- L.N. Dworsky. *Modern transmission line theory and applications*. Wiley, first edition, 1980.
- C.L. Enloe, T.E. McLaughlin, R.D. VanDyken, K.D. Kachner, E.J. Jumper, and T.C. Corke. Mechanisms and Responses of a Single Dielectric Barrier Plasma Actuator: Plasma Morphology. *AIAA J.*, 42(3):589–594, 2004a. ISSN 00011452. URL <http://www.scopus.com/inward/record.url?eid=2-s2.0-1842450556&partnerID=tZ0tx3y1>.
- C.L. Enloe, T.E. McLaughlin, R.D. VanDyken, K.D. Kachner, E.J. Jumper, T.C. Corke, M. Post, and O. Haddad. Mechanisms and Responses of a Single Dielectric Barrier Plasma Actuator: Geometric Effects. *AIAA J.*, 42(3):595–604, 2004b. ISSN 00011452. URL <http://www.scopus.com/inward/record.url?eid=2-s2.0-1842607390&partnerID=tZ0tx3y1>.
- M. Forte, J. Jolibois, J. Pons, E. Moreau, G. Touchard, and M. Cazalens. Optimization of a dielectric barrier discharge actuator by stationary and non-stationary measurements of the induced flow velocity: application to airflow control. *Exp. Fluids*, 43(6):917–928, aug 2007. ISSN 0723-4864. doi: 10.1007/s00348-007-0362-7. URL <http://www.scopus.com/inward/record.url?eid=2-s2.0-36448939101&partnerID=tZ0tx3y1>.
- M. Gad-el Hak. *Flow control: passive, active, and reactive flow management*. Cambridge University Press, 2000.
- D. V. Gaitonde, M. Sahin, K. Shaler, B. Glaz, and S. P G Dinavahi. High-Fidelity simulations of NS-DBD-based control of a stalled NACA0015 airfoil. In *51st AIAA Aerosp. Sci. Meet. Incl. New Horizons Forum Aerosp. Expo. 2013*, 2013. ISBN 9781624101816. URL <http://www.scopus.com/inward/record.url?eid=2-s2.0-84881441947&partnerID=tZ0tx3y1>.
- A. V. Kazakov and M. N. Kogan. Stability of subsonic laminar boundary layer on a flat plate with volume energy supply. *Fluid Dyn.*, 23(2):211–215, 1988. ISSN 0015-4628. doi: 10.1007/BF01051889. URL <http://www.scopus.com/inward/record.url?eid=2-s2.0-0024078949&partnerID=tZ0tx3y1>.

- J.H. Kim, M. Nishihara, I. V. Adamovich, M. Samimy, S. V. Gorbатов, and F. V. Pliavaka. Development of localized arc filament RF plasma actuators for high-speed and high Reynolds number flow control. *Exp. Fluids*, 49(2):497–511, jan 2010. ISSN 0723-4864. doi: 10.1007/s00348-010-0819-y. URL <http://www.scopus.com/inward/record.url?eid=2-s2.0-80053577994&partnerID=tZ0tx3y1>.
- E.E. Kunhardt. Electrical breakdown of gases - the prebreakdown stage. *IEEE Trans. Plasma Sci.*, PS-8(3):130–138, 1980. ISSN 00933813. URL <http://www.scopus.com/inward/record.url?eid=2-s2.0-0019057184&partnerID=tZ0tx3y1>.
- E.E. Kunhardt. Generation of large-volume, atmospheric-pressure, nonequilibrium plasmas. *IEEE Trans. Plasma Sci.*, 28(1):189–200, 2000. ISSN 00933813. doi: 10.1109/27.842901. URL <http://www.scopus.com/inward/record.url?eid=2-s2.0-0033730266&partnerID=tZ0tx3y1>.
- J.C. Lecordier, L.W.B. Browne, S. Le Masson, F. Dumouchel, and P. Paranthoën. Control of vortex shedding by thermal effect at low Reynolds numbers. *Exp. Therm. Fluid Sci.*, 21(4): 227–237, may 2000. ISSN 08941777. doi: 10.1016/S0894-1777(00)00007-8. URL <http://www.scopus.com/inward/record.url?eid=2-s2.0-0034125899&partnerID=tZ0tx3y1>.
- V. A. Levin and O. B. Larin. Skin-friction reduction by energy addition into a turbulent boundary layer. In *41st Aerosp. Sci. Meet. Exhib.*, 2003. ISBN 9781624100994. URL <http://www.scopus.com/inward/record.url?eid=2-s2.0-84882946381&partnerID=tZ0tx3y1>.
- H. W. Liepmann and D. M. Nosenchuck. Active control of laminar-turbulent transition., 1982. ISSN 00221120. URL <http://www.scopus.com/inward/record.url?eid=2-s2.0-0020125458&partnerID=tZ0tx3y1>.
- N. Lin, H.L. Reed, and W.S. Saric. *Instability, Transition, and Turbulence*, chapter Effect of Leading-Edge Geometry on Boundary-Layer Receptivity to Freestream Sound, pages 421–440. Springer New York, 1992.
- J. Little, K. Takashima, M. Nishihara, I. Adamovich, and M. Samimy. Separation control with nanosecond-pulse-driven dielectric barrier discharge plasma actuators. *AIAA Journal*, 50(2):350–365, 2012. doi: 10.2514/1.J051114. URL <http://www.scopus.com/inward/record.url?eid=2-s2.0-84857430467&partnerID=40&md5=c9ca142505d98269589ce8520f9a9a84>.
- T. Log and S. E. Gustafsson. Transient plane source (TPS) technique for measuring thermal transport properties of building materials. *Fire Mater.*, 19(1):43–49, 1995. ISSN 03080501. URL <http://www.scopus.com/inward/record.url?eid=2-s2.0-0029196768&partnerID=tZ0tx3y1>.
- T. Michelis, G. Correale, I. B. Popov, M. Kotsonis, D. Ragni, S. J K Hulshoff, and L. L M Veldhuis. Disturbance introduced into a laminar boundary layer by a NS-DBD plasma actuator. In *51st AIAA Aerosp. Sci. Meet. Incl. New Horizons Forum Aerosp. Expo. 2013*, 2013. ISBN 9781624101816. URL <http://www.scopus.com/inward/record.url?eid=2-s2.0-84881392605&partnerID=tZ0tx3y1>.

- E. Moreau. Airflow control by non-thermal plasma actuators. *Journal of Physics D: Applied Physics*, 40(3):605–636, 2007. URL <http://www.scopus.com/inward/record.url?eid=2-s2.0-33947634508&partnerID=tZ0tx3y1>.
- S. Nagaraja and V. Yang. Energy coupling in repetitively pulsed nanosecond dielectric barrier discharges in plane-to-plane geometry. In *51st AIAA Aerosp. Sci. Meet. Incl. New Horizons Forum Aerosp. Expo. 2013*, 2013. ISBN 9781624101816. URL <http://www.scopus.com/inward/record.url?eid=2-s2.0-84881432597&partnerID=tZ0tx3y1>.
- D.F. Opaitis, A.V. Likhanskii, G. Neretti, S. Zaidi, M.N. Shneider, R.B. Miles, and S.O. Macheret. Experimental investigation of dielectric barrier discharge plasma actuators driven by repetitive high-voltage nanosecond pulses with dc or low frequency sinusoidal bias. *J. Appl. Phys.*, 104(4):043304, 2008. ISSN 00218979. doi: 10.1063/1.2968251. URL <http://www.scopus.com/inward/record.url?eid=2-s2.0-50849098839&partnerID=tZ0tx3y1>.
- I Popov and S Hulshoff. Numerical Investigation of Instabilities in Free Shear Layer Produced by ns-DBD Actuator. *World Acad. Sci. Eng. Technol.*, 68(2012-08-21):1349–1357, 2012.
- N. A. Popov. Investigation of the mechanism for rapid heating of nitrogen and air in gas discharges. *Plasma Phys. Reports*, 27(10):886–896, oct 2001. ISSN 1063-780X. doi: 10.1134/1.1409722. URL <http://www.scopus.com/inward/record.url?eid=2-s2.0-0035538637&partnerID=tZ0tx3y1>.
- H.L. Reed and W.S. Saric. Attachment-line heating in a compressible flow. *J. Eng. Math.*, 84(1):99–110, aug 2013. ISSN 0022-0833. doi: 10.1007/s10665-013-9662-5. URL <http://www.scopus.com/inward/record.url?eid=2-s2.0-84883063375&partnerID=tZ0tx3y1>.
- C. Rethmel, J. Little, K. Takashima, A. Sinha, I. Adamovich, and M. Samimy. Flow separation control using nanosecond pulse driven dbd plasma actuators. *International Journal of Flow Control*, 3(4):213–232, 2011. doi: 10.1260/1756-8250.3.4.213. URL <http://www.scopus.com/inward/record.url?eid=2-s2.0-84870930515&partnerID=40&md5=1bfd1c565fc0247b290427f54145fe29>.
- D. V. Roupassov, A. A. Nikipelov, M. M. Nudnova, and A. Yu. Starikovskii. Flow Separation Control by Plasma Actuator with Nanosecond Pulsed-Periodic Discharge. *AIAA J.*, 47(1): 168–185, jan 2009. ISSN 0001-1452. doi: 10.2514/1.38113. URL <http://www.scopus.com/inward/record.url?eid=2-s2.0-58149522266&partnerID=tZ0tx3y1>.
- M. Samimy, I. Adamovich, B. Webb, J. Kastner, J. Hileman, S. Keshav, and P. Palm. Development and characterization of plasma actuators for high-speed jet control. *Exp. Fluids*, 37(4):577–588, aug 2004. ISSN 0723-4864. doi: 10.1007/s00348-004-0854-7. URL <http://www.scopus.com/inward/record.url?eid=2-s2.0-7044272603&partnerID=tZ0tx3y1>.
- G.S. Settles. *Schlieren and shadowgraph techniques: visualizing phenomena in transparent media*. Springer, 2001.
- A Yu Starikovskii, A A Nikipelov, M M Nudnova, and D V Roupassov. SDBD plasma actuator with nanosecond pulse-periodic discharge. *Plasma Sources Sci. Technol.*, 18(3):034015, aug 2009. ISSN 0963-0252. doi: 10.1088/0963-0252/18/3/034015. URL <http://www.scopus.com/inward/record.url?eid=2-s2.0-68549133419&partnerID=tZ0tx3y1>.

- K. Takashima, Z. Yin, and I.V Adamovich. Measurements and kinetic modeling of energy coupling in volume and surface nanosecond pulse discharges. *Plasma Sources Sci. Technol.*, 22(1):015013, feb 2013. ISSN 0963-0252. doi: 10.1088/0963-0252/22/1/015013. URL <http://www.scopus.com/inward/record.url?eid=2-s2.0-84874027595&partnerID=tZ0tx3y1>.
- T Unfer and J P Boeuf. Modelling of a nanosecond surface discharge actuator. *J. Phys. D. Appl. Phys.*, 42(19):194017, oct 2009. ISSN 0022-3727. doi: 10.1088/0022-3727/42/19/194017. URL <http://www.scopus.com/inward/record.url?eid=2-s2.0-70350626745&partnerID=tZ0tx3y1>.
- F.M. White. *Viscous Flows*. McGraw-Hill, third edition, 2006.
- R. Winkel, G. Correale, and M. Kotsonis. Effect of dielectric material on thermal effect produced by ns-DBD plasma actuator. In *45th AIAA Plasmadynamics Lasers Conf.* American Institute of Aeronautics and Astronautics Inc., 2014. ISBN 9781624102905. URL <http://www.scopus.com/inward/record.url?eid=2-s2.0-84903783466&partnerID=tZ0tx3y1>.
- Y. Wu, Y. Li, H. Liang, and J. Li. Nanosecond pulsed discharge plasma actuation: Characteristics and flow control performance. In *45th AIAA Plasmadynamics Lasers Conf.* American Institute of Aeronautics and Astronautics Inc., 2014. ISBN 9781624102905. URL <http://www.scopus.com/inward/record.url?eid=2-s2.0-84903761289&partnerID=tZ0tx3y1>.
- J.G. Zheng, Z.J. Zhao, J. Li, Y.D. Cui, and B.C. Khoo. Numerical simulation of nanosecond pulsed dielectric barrier discharge actuator in a quiescent flow. *Physics of Fluids*, 26(3), 2014. doi: 10.1063/1.4867708. URL <http://www.scopus.com/inward/record.url?eid=2-s2.0-84903777031&partnerID=40&md5=b91b1f4fe00e380dcda94a1b3f3b6bf7>.
- Y. Zhu, Y. Wu, W. Cui, Y. Li, and M. Jia. Modelling of plasma aerodynamic actuation driven by nanosecond SDBD discharge. *J. Phys. D. Appl. Phys.*, 46(35):355205, sep 2013. ISSN 0022-3727. doi: 10.1088/0022-3727/46/35/355205. URL <http://www.scopus.com/inward/record.url?eid=2-s2.0-84882738466&partnerID=tZ0tx3y1>.

